

Development of a Tunable Diode Laser Absorption Spectroscopy Mass-Flux Sensor for Quantifying Hydrocarbon Storage Tank Venting

by

Simon A. Festa-Bianchet

A thesis submitted to The Faculty of Graduate Studies and Research

in partial fulfilment of the degree requirements of

Master of Applied Science

in

Mechanical Engineering

Ottawa-Carleton Institute for

Mechanical and Aerospace Engineering

Department of Mechanical and Aerospace Engineering

Carleton University

Ottawa, Ontario, Canada

Copyright © 2016 – Simon A. Festa-Bianchet

Abstract

Fixed-roof liquid hydrocarbon storage tanks are a recognized source of volatile organic compounds and greenhouse gases. However, current emissions estimates suffer from a lack of reliable models due to poor in situ validation. This work presents the development and characterization of an intrinsically safe, low velocity mass-flux sensor for monitoring storage tank venting. The sensor is based on tunable diode laser absorption spectroscopy (TDLAS) with wavelength modulation. Similar sensors have been successfully used to measure high velocity flows, such as shock propagation and scramjet combustor exhaust. The oxygen within the vapour space of fixed-roof storage tanks is targeted in the near-IR as the absorption species. Sensor design, optimum operational parameters, and indoor characterization results are presented. An oxygen concentration precision of greater than 0.11% absolute was achieved over the tested range of 2.5 to 21% O₂. For measurements at 21% O₂, a velocity standard deviation of 0.24 m/s for 30-s average measurements was achieved, which could be improved to 0.07 m/s with a 10-minute interval drift correction. However, the velocity measurement accuracy was poor at lower O₂ concentrations, restricting the mass flux capability of the current system.

Acknowledgements

I would like to thank my supervisor Matthew Johnson for his guidance in navigating the ups and downs that have led to today. I consider myself lucky to have worked with someone so passionate about their research.

I would also like to thank David Tyner for seemingly always being there for those same ups and downs in the lab, where they are better referred to as eureka moments and dead-ends. His hands-on attitude and drive to simply get it done were indispensable in the progress of this project. If only it were easier to get a photo of the apparatus without one of his coffee cups in the background.

I would also like to thank Stephen Schoonbaert for his hand in what I have learned in the last few years. His knowledge on everything from lasers to LabVIEW programming (debugging) was invaluable.

I would also like to thank Darcy Corbin for his invaluable help on the manufacturing front, and managing with our vague instructions.

A special thank you to my parents for instilling in me the desire to push the boundaries of what is known about this world. You guys get the cheesy one.

Finally, thank you to Carly for believing in what I do and pushing me through the harder bits. Who knew trail mix could write a thesis?

Table of Contents

Abstract.....	ii
Acknowledgements.....	iii
List of Tables	vi
List of Figures.....	vii
Nomenclature.....	x
Chapter 1 Introduction.....	1
1.1 Background	1
1.2 Current Emission Estimates and Monitoring.....	4
1.3 Field Measurements of Tank Emissions	4
1.4 Thesis Motivation & Objectives	5
1.5 Thesis Outline	7
Chapter 2 Species Flux Measurements Via Tunable Diode Laser Absorption Spectroscopy... 8	
2.1 Spectroscopic Measurement of Light Absorption by Targeted Molecules.....	9
2.1.1 Tunable Diode Laser Absorption Spectroscopy (TDLAS).....	10
2.1.1.1 Sweep Integration	11
2.1.1.2 Wavelength Modulation Spectroscopy.....	12
2.2 Doppler Velocity Calculation.....	16
2.2.1 Review of Doppler Shift Velocity Measurements by TDLAS	19
2.3 Absorption Peak Selection	26
2.3.1 Absorption by O ₂ and other interfering species near 764 nm.....	27
Chapter 3 Experimental Setup.....	29
3.1 General Description.....	29
3.2 Laser Diode	30
3.3 Laser Controller.....	31
3.4 Photodetectors	32
3.5 Optical Setup.....	32
3.5.1 Single Mode Fiber & Splitters	32
3.5.2 Fiber Ring Resonator	34
3.5.3 Oxygen Reference Cell.....	35
3.5.4 Thermal Stability	36
3.5.5 Launch – Fibers & Collimators.....	36

3.5.6	Receive – Fibers, Collimators & Detectors	37
3.6	OTEMS Remote Sample Pipe.....	38
3.6.1	Overview.....	38
3.6.2	Sample pipe.....	39
3.6.3	Windows	40
3.6.4	End Caps	41
3.6.5	Optics Mounting Platforms.....	43
3.6.6	Pressure and Temperature Sensors	43
3.6.7	Explosion Proof Box.....	44
3.7	Mass Flow Controllers	46
3.8	Data Acquisition.....	46
3.8.1	Host Computer – PXI Chassis	46
3.8.2	Field Programmable Gate Array (FPGA).....	47
3.8.3	Frequency Generators	48
3.8.4	Serial Interface	48
3.9	Data Processing	49
3.9.1	Pre-Run System Calibration	49
3.9.1.1	Wavelength Characterization	50
3.9.1.2	Laser Intensity and Phase Characterization.....	52
3.9.2	Velocity Measurement	53
3.9.2.1	Cross-Correlation Velocity.....	54
3.9.3	Concentration.....	56
Chapter 4	Results and Discussion	58
4.1	Optimal Laser Operational Parameters	58
4.2	Digital Filter Selection	61
4.3	End Cap Nitrogen Purging	63
4.4	Velocity Measurement Bias and Drift.....	64
4.5	Velocity Calibration	67
4.6	Concentration Calibration	69
4.7	Mass Flux Results	70
Chapter 5	Conclusions.....	76
5.1	Future Considerations	77
References	79
Appendix A	: Optimization Study	84

List of Tables

Table 2.1: Performance of TDLAS Velocity Systems.....	21
---	----

List of Figures

Figure 1.1: Diagram of a typical fixed roof storage tank. Identified at the top of the tank is the breather vent through which the emissions discussed in the present work are released. Figure reproduced from US EPA (2006) 3

Figure 2.1: Schematic of the laser beam configuration used in OTEMS, simplified to only two lines. Line 1 propagates with the flow direction U while Line 2 counter propagates in the opposite direction. Both lines are launched and collected by collimators, before being sent over fiber optic to their respective detectors. Yellow launch fibers are single mode, while orange return fibers are multi mode. Flow direction is reversible..... 17

Figure 2.2: Idealized $2f$ signals from two counter propagating beams in a flow, demonstrating the Doppler shift in their absorption frequency. The unshifted feature is shown for reference as a dashed grey line. 18

Figure 2.3: a) Absorption of oxygen from 13075 to 13110 cm^{-1} at 21% concentration. 25°C, 1 bar, and a path length of 1.57 m, target absorption line for OTEMS circled in red at a center frequency of 13084.21 cm^{-1} . b) Absorption of common atmospheric gases (water 31690 ppm, carbon dioxide 400 ppm, and methane 2 ppm) from 13075 to 13110 cm^{-1} at 25°C, 1 bar, and a path length of 1.57 m. 28

Figure 3.1: Photograph of the complete OTEMS in an earlier stage of development. The three PelicanTM cases on the right are the base station, while the metal structure on the granite table is the sample pipe. Note that the end caps are not installed. The explosion proof box, detailed in Section 3.6.7, is included in the upper left corner. The contents of this box are seen in front of the sample pipe on the granite table..... 30

Figure 3.2: Diagram of fiber optic network used to tap optical power from the laser diode for the reference cell, laser reference, and fiber ring resonator (also shown in diagram) 33

Figure 3.3: Render of the sample pipe with the inlet and outlet elbows and faceplates 39

Figure 3.4: Render of the sample pipe with the welded box surrounding it 40

Figure 3.5: Early prototype of the end caps, manufactured with clear plastic. Visible through the plastic are single mode launch fibers in yellow and capture multimode fibers in orange..... 42

Figure 3.6: Photograph of one end of the sample pipe. The InvarTM end cap is visible behind its mounting plate. The two launch single mode fibers in yellow and the capture multi-mode fibers in black are attached to the mounting plate. The clear plastic tube is the nitrogen purging system, which vents through the gold valve. 42

Figure 3.7: Photograph of the optics mounting platforms from one end of the sample pipe. The collimators, secured in their kinematic mounts, are shown. A stabilizing cross-brace is visible at the rear of the platforms. 43

Figure 3.8: Explosion proof box. Visible at the bottom are four LMR 400 cables, and to the left side is one multi-mode fiber optic cable (red cable gland). Box is shown not bolted shut..... 45

Figure 3.9: a) Time averaged signal of the FRR and laser intensity from a sweep frequency of 50 Hz with an amplitude of 0.1 V. The peaks of the FRR signal are identified by blue points. b) The FRR

peaks in blue from plot a) are equally spaced on the vertical axis by the FSR to recreate the linear wavenumber sweep, with the first peak set to cm^{-1} . The red line is the combination of linear fits for both the leading and lagging sections of the sweep.	51
Figure 3.10: a) Collected $2f$ signal from OTEMS in solid with the corrected signals in dotted line. 0.2 V sweep @50 Hz (effective sweep amplitude of 0.23 cm^{-1}) and 0.28 V modulation @200 kHz. b) Cross-correlation results for both the original and corrected $2f$ signals.	56
Figure 4.1: Surface plots of the parametric optimization of the OTEMS velocity measurement for varying modulation parameters at a fixed sweep of 50 Hz and 0.1 V amplitude. The minimum standard deviation is highlighted by the red point in each sub plot. a) Short SD, minimum of 0.0326 m/s at 200 kHz and 0.28 V. b) Long SD, minimum of 0.011 m/s at 500 kHz and 0.35 V.	60
Figure 4.2: Surface plots of the parametric optimization of the OTEMS velocity measurement for varying sweep parameters at a fixed modulation of 200 kHz and 0.28 V amplitude. The minimum standard deviation is highlighted by the red point in each sub plot. a) Short SD, minimum of 0.0335 m/s at 50 Hz and 0.1 V. b) Long SD, minimum of 0.012 m/s at 200 Hz and 0.06 V.	60
Figure 4.3: Effect of the cut-off frequency on mean $2f$ peak height and velocity when using a zero-phase change Butterworth low pass filter. Chosen filter frequency, 800 Hz, shown by green vertical line.	62
Figure 4.4: Fast Fourier Transform of a $2f$ signal with no averaging. Blue line is the unfiltered signal, red line is filtered with a lowpass cutoff of 800Hz. Cutoff frequency shown as vertical green line. ...	62
Figure 4.5: Unfiltered and filtered (filtering frequency 800Hz) $2f$ signal.....	63
Figure 4.6: Effect of nitrogen purge in the end caps of the interrogation section on collected $2f$ signals. The gray signal is the background signal for the same sample line when the interrogation section is filled with nitrogen.	64
Figure 4.7: Measured velocity (red trace) with 30 s averaging over a period of 20 hours, recorded in quiescent conditions subject to room temperature changes. The green trace has been adjusted by removing the initial velocity bias present in the raw measurement.	65
Figure 4.8: Adjusted velocity measurement with 30 s averaging over a period of 20 hours, recorded in quiescent conditions subject to room temperature changes. The re-zeroed velocity measurement in blue is the same data but with 10 minute long intervals between zeros.	66
Figure 4.9: Mean measured velocity (zero corrected) by the OTEMS with respect to the reference velocity determined by the digital mass flow controllers. Plot a) displays the results from 0 to 6 m/s bulk velocity with a linear line of best fit. Plot b) displays the results from 0 to 2 m/s bulk velocity with the same linear line of best fit as in a). Error bars on both plots are the standard deviation of the 20 data points within each sample.	68
Figure 4.10: Mean measured oxygen mole fraction with respect to reference oxygen mole fraction as determined by the mass flow controllers. Each mole fraction set point was done at 4 flow velocities: 0.5, 1.0, 1.5, and 2.0 m/s.....	70
Figure 4.11: Comparison of measured and specified oxygen mole fractions in the OTEMS during a flux experiment. Dotted green line is the reference mole fraction of oxygen as reported by the MFCs.	71
Figure 4.12: Velocity measurement of the OTEMS during a varied mass flux experiment. Velocities are grouped by colour based on the volume fraction of oxygen during the measurement. The dotted red line is the reference bulk velocity as reported by the MFCs.....	72

Figure 4.13: Error of the mean velocity measurement (from the MFC reference velocity) with changing oxygen mole fraction. The oxygen mole fraction is the MFC reported value. For each mole fraction value, four different velocity values were specified: 0.5, 1.0, 1.5, and 2.0 m/s. Data from two subsequent days is presented..... 73

Figure 4.14: Comparison of the $2f$ signal in two lines for high and low oxygen mole fractions (21% and 2.5% respectively). Subplot b) shows the decreased SNR in the $2f$ signal at 2.5% oxygen relative to 21%. 74

Figure A.1: Surface plots of the parametric optimization of the OTEMS velocity measurement for varying modulation parameters at a fixed sweep of 100 Hz and 0.28 V amplitude. The minimum standard deviation is highlighted by the red point in each sub plot. a) Short SD, minimum of 0.0386 m/s at 320 kHz and 0.5 V. b) Long SD, minimum of 0.008 m/s at 320 kHz and 0.3 V..... 84

Figure A.2: Surface plots of the parametric optimization of the OTEMS velocity measurement for varying sweep parameters at a fixed modulation of 320 kHz and 0.5 V amplitude. The minimum standard deviation is highlighted by the red point in each sub plot. a) Short SD, minimum of 0.0376 m/s at 50 Hz and 0.1 V. b) Long SD, minimum of 0.013 m/s at 50 Hz and 0.12 V..... 85

Figure A.3: Surface plots of the parametric optimization of the OTEMS velocity measurement for varying modulation parameters at a fixed sweep of 50 Hz and 0.1 V amplitude. The minimum standard deviation is highlighted by the red point in each sub plot. a) Short SD, minimum of 0.0326 m/s at 200 kHz and 0.28 V. b) Long SD, minimum of 0.011 m/s at 500 kHz and 0.35 V..... 86

Figure A.4: Surface plots of the parametric optimization of the OTEMS velocity measurement for varying sweep parameters at a fixed modulation of 200 kHz and 0.28 V amplitude. The minimum standard deviation is highlighted by the red point in each sub plot. a) Short SD, minimum of 0.0335 m/s at 50 Hz and 0.1 V. b) Long SD, minimum of 0.012 m/s at 200 Hz and 0.06 V. 86

Nomenclature

Latin Symbol	Description	Units	First Eq.	Use Pg.
a_m	Modulation depth (or amplitude)	cm^{-1}	2.6	13
a_{sweep}	Sweep amplitude	cm^{-1}		35
b	Harmonic integer	-	2.8	14
c	Speed of light in a vacuum, $c = 299,792,458$	m/s	2.17	16
f_f	Filter cut-off frequency	Hz		61
f_m	Modulation frequency	Hz	2.5	13
f_{samp}	Sampling frequency	Hz		16
f_{sweep}	Sweep frequency	Hz		12
g	Line shape of an absorption line	cm	2.2	10
H_b	Fourier coefficients	-	2.8	14
I	Measured light intensity with absorption	V	2.1	9
I_0	Measured light intensity without absorption	V	2.1	13
\bar{I}_0	Average measured light intensity without absorption	V	2.5	13
\bar{I}_{0ref}	Average measured light intensity without absorption of the laser reference line	V		52
i_0	Linear intensity modulation amplitude, normalized by \bar{I}_0	-	2.5	13
i_{0ref}	Linear intensity modulation amplitude of the laser reference, normalized by \bar{I}_{0ref}	-		52
i_2	Second harmonic light intensity modulation amplitude, normalized by \bar{I}_0	-	2.5	13
i_{2ref}	Second harmonic light intensity modulation amplitude of laser reference, normalized by \bar{I}_{0ref}	-		52
k	Boltzmann constant, $k = 1.380658 \times 10^{-19}$	$\text{kg} \cdot \text{cm}^2/\text{s}^2 \cdot \text{K}$	2.1	9
L	Path length of absorption	m	2.1	9
L_{FRR}	Half circumference of Fibre Ring Resonator	m	3.1	34
M	Number of sample points within one modulation period	-	2.14	15
\mathbb{N}	Set of natural numbers	-	2.10	14
n_e	Effective index of refraction	-	3.1	35
p	Pressure	Pa	2.1	9
q	Volume mixing ratio	-	2.1	9
q_j	Volume mixing ratio of molecule j	-	2.3	10
R_{xy}	Cross-correlation of x and y	-	3.3	54
R_{2f}	Second harmonic signal, root-sum-of-squares of X and Y components	V	2.13	14
$R_{2f_1}^2$	Squared second harmonic signal of sample line 1	V^2	3.2	47
S	Line strength of an absorption line	cm/molecule	2.2	10
T	Temperature	K	2.1	9
U	Bulk flow velocity	m/s	2.17	16
X_{2f}	X component of second harmonic	V	2.11	15

Latin Symbol	Description	Units	First Eq.	Use Pg.
x	Signal x used in cross-correlation	-	3.3	54
x^*	Complex conjugate of signal x used in cross-correlation	-	3.3	54
x_1	Detector voltage of sample line 1	V	3.2	47
$x_{O_2,V}$	Mole fraction of oxygen in the tank vapour mixture	%	2.19	27
$x_{O_2,\infty}$	Mole fraction of oxygen in ambient air	%	2.19	27
x_{vapour}	Mole fraction of hydrocarbon vapours	-	2.19	27
y	Signal y used in cross-correlation	-	3.3	54
Y_{2f}	Y component of second harmonic	V	2.12	15
$2f$	Second harmonic signal	V		12

Greek Symbol	Description	Units	First Eq.	Use Pg.
α	Absorption	-	2.4	10
η	Simplifying variable, $2\pi ft$	rad	2.8	14
θ	Angle between beams in sample tube for Doppler shift	rad	2.17	16
ν	Frequency	cm ⁻¹	2.1	10
ν_c	Center frequency of an absorption line	cm ⁻¹	2.2	9
ν_0	Unshifted frequency	cm ⁻¹	2.17	16
$\bar{\nu}$	Average frequency	cm ⁻¹	2.6	13
$\Delta\nu$	Doppler frequency shift	cm ⁻¹	2.17	16
$\frac{\Delta\nu_{12}}{\Delta\nu_{12}}$	Doppler frequency shift between lines 1 and 2	cm ⁻¹	2.18	18
$\Delta\nu_{12}$	Average Doppler frequency shift between lines 1 and 2	cm ⁻¹		53
$\Delta\nu_{12,lead}$	Leading Doppler frequency shift between lines 1 and 2	cm ⁻¹		
π	Constant, 3.14159	-	2.5	13
ψ_1	Phase-shift between the linear modulation intensity and wavelength signals	rad	2.5	13
ψ_{1ref}	Phase-shift between the linear modulation intensity of the laser reference line and wavelength signals	rad		52
ψ_2	Phase-shift between the second order modulation intensity and wavelength signals	rad	2.5	13
ψ_{2ref}	Phase-shift between the second order modulation intensity of the laser reference line and wavelength signals	rad		52
σ	Standard deviation	various		22
σ_{ν_c}	Absorption cross-section of an absorption line at ν_c	cm ² /molecule	2.1	9
$\sigma_{\nu_c^{i,j}}$	Absorption cross-section of an absorption line i at ν_c of a molecule j	cm ² /molecule	2.3	10
τ	Transmittance	-	2.3	9
τ_{ν_c}	Transmittance of absorption line at center frequency ν_c	-	2.1	9

Acronyms	Description	First Eq.	Use Pg.
AC	Alternating Current		
AER	Alberta Energy Regulator		1

Acronyms	Description	First Use Pg.
API	American Petroleum Institute	1
AP-42	Compilation of Air Pollutant Emission Factors	4
AR	Anti-Reflective	36
CSA	Formerly Canadian Standards Association, now CSA Group	37
cw	Continuous Wave	24
DA	Direct Absorption	10
DAQ	Data Acquisition	45
DC	Direct Current	36
DFB	Distributed Feedback Diode	26
DIAL	Differential Absorption LIDAR	1
DPG	Digital Pressure Gauge	44
EPA	Environmental Protection Agency	2
FC/APC	Ferrule Connector Angled Physical Contact	31
FGEN	Frequency Generators	48
FPGA	Field Programmable Gate Array	29
FRR	Fiber Ring Resonator	34
FSR	Free Spectral Range, cm^{-1}	34
FWHM	Full-Width at Half-Maximum	18
GHG	Greenhouse Gas	1
HITRAN	High-Resolution Transmission Molecular Absorption Database	10
HWHM	Half-Width at Half-Maximum	30
IO	Input and Output	46
LabVIEW	Laboratory Virtual Instrument Engineering Workbench	46
Laser	Light Amplification by Stimulated Emission of Radiation	6
LDV	Laser Doppler Velocimetry	19
LIDAR	Light Detection and Ranging	1
LPM	Litres per Minute	46
Maser	Microwave Amplification by Stimulated Emission of Radiation	8
MFC	Mass Flow Controller	44
MM	Multi-mode	38
MPMS	Manual of Petroleum Measurement Standards	4
N/A	Not Available	21
Near-IR	Near infrared spectroscopic region (700-2500 nm)	27
NPSM	National Pipe Straight Mechanical	44
NPT	National Pipe Thread	41
OTEMS	Optical Tanks Emissions Measurement System	6
PDS	Photothermal Deflection Spectroscopy	19
PXI	PCI eXtensions for Instrumentation	46
RAM	Residual Amplitude Modulation	13
SD	Standard Deviation	21
SI	Sweep Integration	11
SLPM	Standard Litres per Minute (variable standards)	46

Acronyms	Description	First	Use
			Pg.
SNR	Signal-to-noise-ratio		12
STP	Standard temperature (288.15 K) and pressure (101.325 kPa)		9
TDL	Tunable Diode Laser		12
TDLAS	Tunable Diode Laser Absorption Spectroscopy		7
TEC	Thermo-electric cooler/heater		31
TTV	Transit Time Velocimetry		19
USB	Universal Serial Bus		31
VCSEL	Vertical Cavity Surface Emitting Laser		26
VI	Virtual Instrument		50
VOC	Volatile Organic Compound		1
WMS	Wavelength Modulation Spectroscopy		12
WMS – $2f$	Wavelength Modulation Spectroscopy with second harmonic detection		22
WMS – $2f/1f$	Wavelength Modulation Spectroscopy with second harmonic detection with first harmonic normalization		23
Chemical Formulae	Description	First	Use
			Pg.
AlGaAs	Aluminium gallium arsenide		25
Ar	Argon		21
C ₂₊	Hydrocarbons with 2 or more carbon atoms		1
CH ₄	Methane		1
CO ₂	Carbon dioxide		1
CO _{2e}	Carbon dioxide equivalent		1
H ₂	Hydrogen		22
He	Helium		21
H ₂ O	Water		22
Si	Silicone		25
N ₂	Nitrogen		64
Ne	Neon		21
NO	Nitric oxide		21
O ₂	Oxygen		10
OH	Hydroxide		21

Chapter 1 Introduction

1.1 Background

Atmospheric pressure liquid hydrocarbon storage tanks are used in all sectors of the energy industry. However, emissions of volatile organic compound (VOC) and greenhouse gases (GHG) from these tanks are poorly understood. There is mounting evidence that emissions from liquid storage tanks are cause for concern and may represent a significant fraction of total industry VOC emissions. A 2008 study conducted in Alberta using differential absorption LIDAR (DIAL) found that 50% of total site emissions of C₂₊ hydrocarbons and benzene were attributable to the storage tank area (Chambers et al., 2008). A recent inquiry by the Alberta Energy Regulator (AER) identified heated liquid storage tanks as the principal source of odour releases in the Peace River area (AER, 2014). Exploratory measurements at a downstream commercial gasoline station suggested that temperature differentials between the hydrocarbon liquid in an underground gasoline tank and ambient air drawn in through the vent line of the tank led to a doubling of VOC emissions relative to standard models used in emissions reporting (Picard and Johnson, 2011).

According to the 2011 Canadian national greenhouse gas emissions inventory, which focuses on CO₂ and CH₄, the contribution of storage tank losses was 792,500 tonnes of CO₂e in 2010. These values were derived using API emission estimating procedures (Clearstone Engineering Ltd., 2014a), which are further outlined in Section 1.2. The same inventory also outlines that the majority of hydrocarbon storage tanks in Canada are of fixed-roof construction,

in which the liquid is stored in a closed, atmospheric pressure tank that typically vents directly to atmosphere to prevent pressure differentials across the tank walls. A minority of tanks, typically large tanks at distribution centers, are of the floating-roof type, in which a movable roof rests on the liquid surface and employs various types of wiper seals to the walls of the tank to help suppress evaporative emissions.

The present work focuses solely on fixed-roof storage tanks. A diagram of such a tank, reproduced from US EPA (2006), is shown in Figure 1.1. Fixed-roof storage tanks are maintained at atmospheric pressure through a breather vent located on their roof. This vent allows for the free exchange of gases between the inside of the tank and its surroundings. Fixed-roof liquid storage tanks exhibit three principal types of losses: flashing, working, and standing losses. The total emission from an individual tank is the sum of these different losses. Flashing losses occur when liquid at slightly elevated pressure is pumped into an atmospheric pressure tank and the incurred sudden pressure drop allows dissolved gases to be released from the liquid phase. In general, flashing losses are best controlled by upstream operating decisions to avoid directing pressurized liquid to atmospheric liquid storage tanks. Working losses are a result of an expulsion of vapours when the tanks are being loaded with additional product (i.e. due to liquid level changes within the tank pushing out an equal volume of vapours from the tank ‘head space’). Standing losses are the result of a diurnal breathing cycle, in which the cycle of daytime heating and nighttime cooling causes the vapour within the tank to expand and contract. This results in the expulsion of an air and hydrocarbon vapour mixture containing elevated concentrations of VOCs from the stored product.

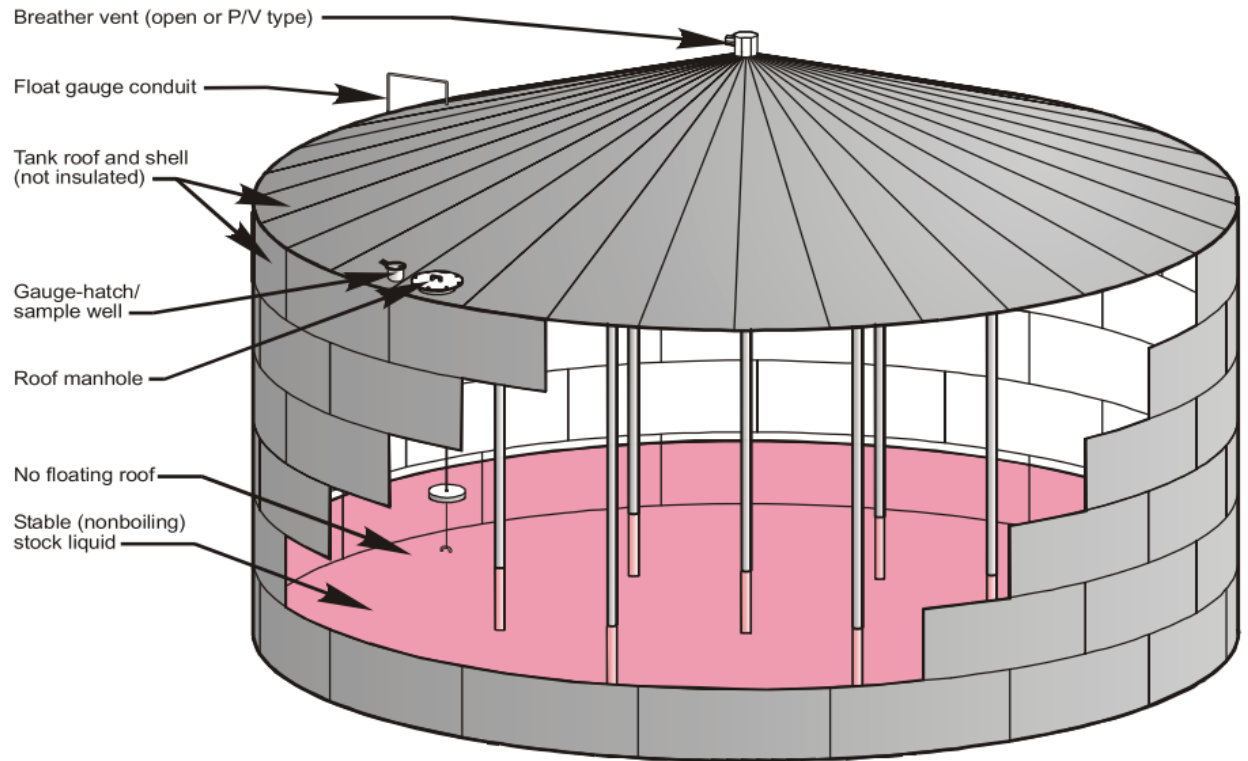


Figure 1.1: Diagram of a typical fixed roof storage tank. Identified at the top of the tank is the breather vent through which the emissions discussed in the present work are released. Figure reproduced from US EPA (2006)

Exploratory results have suggested that these breathing losses are exacerbated when there is a temperature differential such that the stored liquid is warmer than the ambient air (Picard and Johnson, 2011). Convective mixing driven by this temperature difference is thought to increase the concentration of VOCs in the tank head space leading to augmented emissions. This potential issue is of special concern in Canada where heated and/or insulated tanks are often employed in the upstream oil industry, and ambient temperatures are often lower than that of the stored hydrocarbon liquid.

While there is no official inventory of storage tanks in Canada, an estimate based on typical site configurations (Clearstone Engineering Ltd., 2014b) and published active facility lists in Alberta (AER, 2015) and Saskatchewan (Saskatchewan Ministry of Economy, 2015) puts

the number of fixed roof tanks in the Canadian upstream oil and gas industry at more than 80,000. This figure does not include fixed roof tanks used in the downstream industry, which are found in numerous applications from chemical refinery plants, to agricultural applications, to local gasoline stations countrywide.

1.2 Current Emission Estimates and Monitoring

Currently, most estimates of emissions from liquid hydrocarbon storage tanks rely on a set of semi-empirical equations found within chapter 7 of the U.S. Environmental Protection Agency's (EPA) AP-42 (US EPA, 2006). The equations and factors relating to hydrocarbon storage tanks were originally developed, and copyrighted, by the American Petroleum Institute (API). The API also publishes their own model within their Manual of Petroleum Measurement Standards (MPMS), in chapter 19.1 (Ferry and Kissell, 2010). The process to develop these equations started over 60 years ago, and many components have not been updated in decades due to a lack of new insight. Certain factors in the model, such as the turnover factor relating to the frequency of filling events, are solely based on values proposed by industry representatives as far back as 1952. When supporting data are available, they are limited in scope and questionable in accuracy. A passage from the conference proceedings of the annual API symposium is just as relevant today as it was at the time: "It seems as though in evaporation-loss work there is a wider abundance of opinions, in contrast to a marked scarcity of facts, than is the case in most studies having a technical background" (American Petroleum Institute, 1952).

1.3 Field Measurements of Tank Emissions

The field measurements of emissions from storage tanks upon which AP-42 is based all share a common limitation of relying on concentration measurements made over short periods of time.

The most common methodology is to multiply measured vent flow rates by a single measurement of VOC concentration. This VOC concentration would be taken once per day using a bag sample method. The measured flow rates were usually collected using turbine flow meters installed on the tank's vent, which were operated for single day periods (API, 1993). To account for varying VOC concentrations, the published model uses various concentration factors. A time sensitive pairing of flow rate and VOC concentration would allow for a better understanding of the dynamic problem which is storage tank venting losses. To date, only a single study has attempted such a paired measurement (Picard and Johnson, 2011). An underground gasoline storage tank was instrumented with an ultrasonic flow meter and an electrochemical gas sensor to simultaneously measure flow velocity and oxygen concentration respectively. VOC concentrations were then calculated by comparing the oxygen concentration within the vent to atmospheric levels. While this study did provide some provocative comparison with the AP-42 estimates suggesting significantly higher than predicted emissions, it suffered from poor accuracy on the concentration measurements (Picard and Johnson, 2011). In general, electrochemical sensors are subject to cross-contamination bias errors from other species and time-dependent sensitivity degradation. In addition, strict safety protocols at oil and gas facilities limit the use of electronics near liquid storage tanks.

1.4 Thesis Motivation & Objectives

The objective of this thesis is to develop a sensor capable of continuously measuring VOC flux from venting events on fixed roof storage tanks. The inspiration for the technology behind the sensor stems from research conducted in the 1990's and 2000's on inlet mass flux measurements on turbine engines at Stanford University (Lyle, Jeffries, Hanson, et al., 2007; Lyle, 2005). In these studies, an optical sensor was built to probe the presence of oxygen within the inlet stream

to determine both its concentration and velocity in the inlet to a turbine. These two measurements are possible using a single laser diode which can be tuned across a particular frequency range which is absorbed by oxygen. Velocity is calculated from a measured Doppler shift in beams directed across the gas flow. Concentration can be determined by the strength of the observed absorption, which is directly affected by the mass fraction of oxygen in the flow. While these measurements were done with flow velocities ranging from 40 to 175 m/s, low speed wind tunnel tests were conducted between 1 and 23 m/s to validate the sensor. These low speed tests indicated that a 1 s standard deviation in velocity of 0.22 m/s was achievable at atmospheric oxygen concentration levels (Lyle, Jeffries, and Hanson, 2007). Achieving such a low velocity resolution is critical to the success of a vent flux monitoring system, as flow velocities can be expected to remain below 5 m/s during the majority of a tank's operation.

This thesis describes a new sensor system known as OTEMS (Optical Tank Emissions Measurement System), and presents quantitative calibration and performance data from controlled lab testing. Unlike the low speed tests of Lyle, Jeffries, and Hanson (2007), which were conducted by directly irradiating photodetectors, the current work explores the feasibility of re-coupling the light into fiber optic cables. This all-optical design removes all electronic components from the immediate vicinity of the sensor, thereby avoiding significant complications related to electrical safety codes at field sites which are extremely strict in the immediate vicinity of hydrocarbon storage tanks. Additionally, the measurement is non-intrusive and does not affect the venting of the tank. The sensor is simply added as an extension to the breather vent on the tank's roof and adds no significant pressure differential. Ultimately, OTEMS could be used to re-evaluate the models presented in AP-42 and to provide more

accurate hydrocarbon storage tank emissions data to industry operators, engineers, and policy makers.

1.5 Thesis Outline

Chapter 2 presents the theory of Tunable Diode Laser Absorption Spectroscopy and its application to the OTEMS. A tabulated review of previous studies using TDLAS to measure velocity is also presented and discussed. Chapter 3 details the experimental design including the required fiber-optic components, digital data acquisition hardware, and associated data processing techniques. In Chapter 4 the results of an optimization of operational parameters are presented along with a discussion on the current performance of a calibrated OTEMS. Finally, Chapter 5 summarizes conclusions from the thesis and recommendations for future extensions of this work.

Chapter 2 Species Flux Measurements Via Tunable Diode Laser Absorption Spectroscopy

To determine the flux of a species two quantities are required: velocity and concentration. With the use of TDLAS, both of these quantities can be accurately calculated from a single measurement. This chapter provides a detailed overview of the theory for determining these two quantities, beginning with the fundamentals of absorption spectroscopy. The idea of probing gaseous substances with the use of narrow bandwidth light to selectively excite target molecules emerged in the 1960's, in conjunction with the increased availability of coherent light sources that could be tuned to match a target resonance frequency. Some of the first such work was conducted on a ruby maser, which could be tuned by varying its temperature (Abella and Cummins, 1961). This occurred shortly after the first laser was built at the Hughes Research Laboratories by Theodore H. Maiman (1960), inspired by the theoretical derivations of Schawlow and Townes (1958). From there, the applications of laser spectroscopy have been wide and varied. The advent of laser diodes, with a wide range of center frequencies, has led to the development and refinement of a technique generally known as tunable diode laser absorption spectroscopy (TDLAS). The small size and low power consumption of modern laser diodes allow for their integration in nearly all situations and environments. Below is an overview of TDLAS theory and its applications to tank venting losses.

2.1 Spectroscopic Measurement of Light Absorption by Targeted Molecules

At the basis of any spectroscopy measurement is the spectrally-dependant absorption of radiation by a gas molecule or molecules of interest. When a beam of light at a carefully selected wavelength traverses a volume containing a target gas species with a matching resonance frequency, a certain quantity of light will be absorbed by the gas molecules as they are elevated to a higher energy state. The absorbed energy is most often converted into random atomic motion, or kinetic energy, through collisions. Often referred to as dissipative absorption, this returns the molecule to a lower energy state before a photon can be emitted by the molecule (Hecht, 2002). The ratio of light intensities before and after the interrogation (I_0 and I respectively) can be used to determine the volume mixing ratio (also referred to as the volume fraction) of absorbing molecules. This behaviour is described by the Beer-Lambert-Bouguer Law, which relates the transmittance, τ , of light at a specific absorption line at center frequency, ν_c [cm^{-1} , as measured in wavenumbers], to the pressure, p [Pa], temperature, T [K], volume mixing ratio of the absorbing molecule, q [-], and optical path length traversed through the absorbing media, L [m]. The law only applies if scattering effects can be ignored, which is the case for atmospheric gases at STP (Hecht, 2002). The Beer-Lambert-Bouguer Law can be written as follows:

$$\tau_{\nu_c}(\nu) = \frac{I}{I_0} = \exp\left(-\frac{qpL}{kT}\sigma_{\nu_c}(p, T, q, \nu)\right) \quad (2.1)$$

where k is the Boltzmann constant [$1.38064852 \times 10^{-19}$ ($\text{kg}\cdot\text{cm}^2/(\text{s}^2\cdot\text{K})$)] and σ_{ν_c} is the absorption cross-section [$\text{cm}^2/\text{molecule}$] at wavenumber ν_c .

For a single absorption line of a single species, the absorption cross-section can be calculated using tabulated spectroscopic data such as the HITRAN database (Rothman et al., 2009):

$$\sigma_{v_c}(p, T, q, \nu) = S(T, v_c)g(p, T, q, \nu - v_c) \quad (2.2)$$

where $S(T, v_c)$ [cm/molecule] is the line strength of the absorption line at v_c and $g(p, T, q, \nu - v_c)$ [cm] is the line-shape. To accurately describe the transmittance at any particular wavenumber, the sum of all contributing absorption lines neighboring that wavenumber must be considered (Gordley et al., 1994). Equation (2.1) can be generalized as shown in Eq. (2.3) to account for the presence of multiple absorption lines:

$$\tau(\nu) = \frac{I}{I_0} = \exp\left(-\sum_j \sum_i \frac{q_j p L}{kT} \sigma_{v_{c_i}, j}(p, T, q_j, \nu)\right) \quad (2.3)$$

where $\sigma_{v_{c_i}, j}$ is the absorption cross-section of the i^{th} absorption line center of the j^{th} molecule. The principal challenge in any spectroscopy measurement is the accurate measurement of this transmittance, or alternatively the absorption, α :

$$\alpha(\nu) = 1 - \tau(\nu) \quad (2.4)$$

As further discussed in Section 2.3, the OTEMS focuses on the spectral absorption of atmospheric oxygen found within the vent gas of liquid hydrocarbon storage tanks. The selection of a specific O₂ absorption feature for measurement is discussed in Section 2.3.1.

2.1.1 Tunable Diode Laser Absorption Spectroscopy (TDLAS)

Multiple techniques exist under the umbrella of TDLAS. The most basic of these is known as direct absorption (DA), where the absorption of light is measured at a fixed wavelength. This

technique has also been called fixed wavelength absorption. Hiller et al. (1983) derived a technique based on a single DA measurement to determine the velocity of a subsonic nitrogen jet. Davidson et al. (1991) compared a similar DA technique with a tuned frequency method known as sweep integration (SI, described in 2.1.1.1) and concluded that SI leads to a decrease in measurement scatter over DA at a cost of higher data storage requirements. The higher accuracy of tuned frequency methods over a fixed frequency velocity measurement was also reported by Hiller and Hanson (1988).

2.1.1.1 Sweep Integration

As an evolution of the DA method, Sweep Integration (SI) is conducted by scanning the wavelength of the interrogating light source over the center frequency of the absorption line of interest (Jennings, 1980). Depending on the magnitude of the wavelength scan, or sweep, a full or partial measurement of the absorption feature is acquired. The peak absorption can be determined from this measured feature and used to determine the volume fraction of the target species. In addition, as further discussed in Section 2.2, the location of the absorption peak can be compared with the corresponding Doppler-shifted location from a second measurement to infer the bulk gas velocity. An advantage of the SI method is that it requires relatively simple data acquisition equipment and data processing. SI has been used in previous O₂ mass flux experiments with some success (Miller et al., 1996), achieving a mass flux precision and accuracy of 2% of full scale over a range of 29.7 to 94.2 kg/s (65.3 to 207.3 lb/s). However, SI is mostly restricted to strong absorbers which produce an easily measured absorption signal relative to the absorption free intensity. For weak absorbers, SI has largely been replaced by modulation-based techniques or else limited to high concentration measurements (Lyle, Jeffries, and Hanson, 2007; Li et al., 2012).

2.1.1.2 Wavelength Modulation Spectroscopy

In a Wavelength Modulation Spectroscopy (WMS) based measurement system, the wavelength of a tunable laser diode (TDL) is swept back and forth across an absorption feature at frequency (f_{sweep}) while simultaneously superimposing a high frequency sinusoidal wavelength modulation (f_m). Both the slower sweep frequency and the higher modulation frequency are achieved by varying the injection current to the TDL (Reid and Labrie, 1981). WMS with harmonic detection has been recognized as an improvement over sweep integration, because it allows for a significantly increased detection frequency. This is advantageous because the noise power spectral density tends to be inversely proportional to frequency. Previous studies have shown improvements by switching from SI to WMS for velocity measurements using oxygen (Lyle, Jeffries, Hanson, et al., 2007; Philippe and Hanson, 1993).

Harmonic detection extracts components of the intensity after absorption that correspond to multiples of the modulation frequency by exploiting the orthogonality of the sinusoidal modulation. Higher signal-to-noise ratios (SNR) over SI were first reported for harmonic detection with TDLs by Reid et al. (1978) and Reid and Labrie (1981). WMS systems are often configured for second harmonic detection, where the components of the measured return intensity at twice the modulation frequency ($2f_m$) are extracted. First harmonic detection extracts components of the signal matching the modulation frequency ($1f_m$), and has been used previously to normalize the $2f$ signal so as to reduce noise introduced by beam steering and vibrations (Chang et al., 2010).

When describing the intensity and wavelength of the TDL, the slower sweep component is usually neglected as its impact on the second harmonic lineshape (i.e. the measured $2f$ signal,

as further discussed below) is minimal (Olson et al., 1980). The laser output intensity, $I_0(t)$, and frequency, $\nu(t)$ can therefore be written as follows:

$$I_0(t) = \bar{I}_0(1 + i_0 \cos(2\pi f_m t + \psi_1) + i_2 \cos(4\pi f_m t + \psi_2)) \quad (2.5)$$

$$\nu(t) = \bar{\nu} + a_m \cos(2\pi f_m t) \quad (2.6)$$

where \bar{I}_0 is the average laser intensity, i_0 is the amplitude of the linear intensity modulation with phase shift ψ_1 with respect to laser wavelength, i_2 is the first term of the nonlinear intensity modulation with phase shift ψ_2 , f_m is the modulation frequency, $\bar{\nu}$ is the average frequency and a_m is the amplitude of the frequency modulation.

The intensity after absorption can be found by inserting the instantaneous optical frequency into equation (2.3) and rearranging for I :

$$\begin{aligned} I(t) &= I_0(t) \cdot \tau(\nu(t)) \\ &= I_0(t) \cdot \exp\left(-\sum_j \sum_i \frac{q_j p L}{kT} \sigma_{\nu_{c_i j}}(p, T, q_j, \bar{\nu} + a_m \cos(2\pi f_m t))\right) \end{aligned} \quad (2.7)$$

Second harmonic detection is used as it retains lower Residual Amplitude Modulation (RAM) effects (Philippe and Hanson, 1991) with only slightly lower signal intensity over the first harmonic. RAM is a generally unwanted characteristic of TDLs, where the intensity of the laser is unavoidably modulated at the same frequency as the wavelength. This intensity modulation can be comparable in magnitude to the intensity drop due to spectral absorption (Cassidy and Reid, 1982). Additionally, the second harmonic feature ($2f$) is a peak centered on

the original absorption peak location (Bomse et al., 1992) – idealized $2f$ peaks are shown in Figure 2.2. For these reasons, WMS with second harmonic detection was selected for the OTEMS.

By expanding the transmittance in equation (2.7) as a Fourier series, it is possible to derive an expression for the theoretical second harmonic signal. The notation used here is based on (Rieker, 2009). The transmittance, $\tau(v(t))$, can be written as follows by also using the simplifying variable replacement of $\eta = 2\pi f_m t$:

$$\tau(v(\eta)) = \sum_{b=0}^{\infty} H_b(\bar{v}, a_m) \cos(b\eta) \quad (2.8)$$

where the Fourier coefficients are defined as:

$$H_0(\bar{v}, a_m) = \frac{1}{2\pi} \int_{-\pi}^{\pi} \tau(\bar{v} + a_m \cos(\eta)) d\eta \quad (2.9)$$

$$H_b(\bar{v}, a_m) = \frac{1}{\pi} \int_{-\pi}^{\pi} \tau(\bar{v} + a_m \cos(\eta)) \cos(b\eta) d\eta, \quad b \in \mathbb{N} \quad (2.10)$$

By combining this Fourier expansion of the transmittance with the laser output intensity, a model for the detected signal is achieved. The first step to finding an expression for the $2f$ signal (R_{2f}) is to multiply the detected signal by $\cos(2\eta)$ and $\sin(2\eta)$. By integrating over the modulation period, the X and Y components of the second harmonic can then be extracted as shown in Eq. (2.11) and (2.12).

$$\begin{aligned}
X_{2f} &= \frac{1}{2\pi} \int_{-\pi}^{\pi} I_0(\eta) \tau(v(\eta)) \cos(2\eta) d\eta \\
&= \frac{\bar{I}_0}{2} \left(H_2 + \frac{i_0}{2} (H_1 + H_3) \cos(\psi_1) + i_2 \left(H_0 + \frac{H_4}{2} \right) \cos(\psi_2) \right)
\end{aligned} \tag{2.11}$$

$$\begin{aligned}
Y_{2f} &= \frac{1}{2\pi} \int_{-\pi}^{\pi} I_0(\eta) \tau(v(\eta)) \sin(2\eta) d\eta \\
&= -\frac{\bar{I}_0}{2} \left(\frac{i_0}{2} (H_1 - H_3) \sin(\psi_1) + i_2 \left(H_0 - \frac{H_4}{2} \right) \sin(\psi_2) \right)
\end{aligned} \tag{2.12}$$

Both the X and Y components are required to be able to account for the phase misalignment of the laser intensity and wavelength. The $2f$ signal is then the root-sum-square of the X and Y components.

$$R_{2f} = \sqrt{X_{2f}^2 + Y_{2f}^2} \tag{2.13}$$

Experimentally the $2f$ signal is found by approximating the integration over each modulation period j by a Riemann sum, and replacing the product of absorption free intensity and transmittance by the detector signal $I(t_i)$ at each sample point t_i :

$$X_{2f}(j) = \frac{1}{M} \sum_{i=0}^M I(t_i) \cos(4\pi f_m t_i) \tag{2.14}$$

$$Y_{2f}(j) = \frac{1}{M} \sum_{i=0}^M I(t_i) \sin(4\pi f_m t_i) \quad (2.15)$$

In Eq. (2.14) and (2.15), M is the number of sample points within one modulation period, which is dictated by the ratio of the modulation frequency (f_m) to the sampling frequency (f_{samp}). The number of modulation periods j is dictated by the ratio of the modulation frequency to the sweep frequency (f_{sweep}). The resultant experimentally measured $2f$ signal is similarly computed as the root-sum-square of the X and Y components.

$$R_{2f}(j) = \sqrt{X_{2f}(j)^2 + Y_{2f}(j)^2} \quad (2.16)$$

The height of the measured $2f$ peak can then be compared to a look-up table of theoretical peak heights for a given set of environmental conditions to evaluate species concentration. This procedure is further discussed in Section 3.9.3.

2.2 Doppler Velocity Calculation

The Doppler effect will shift the frequency of light absorption by molecules in a fluid with velocity U [m/s] relative to molecules in a stationary fluid according to the following relation:

$$\Delta\nu = \frac{\nu_0 U}{c} \cos(\theta) \quad (2.17)$$

where $\Delta\nu$ [cm^{-1}] is the Doppler frequency shift, c [m/s] is the speed of light, ν_0 [cm^{-1}] is the center frequency of the unshifted absorption line, and θ is the angle between the velocity vector of the molecule and the interrogating laser beam. Maximum sensitivity is achieved when the flow is directly parallel to the laser beam. The Doppler frequency shift can be found by comparing the location of an absorption feature to that of an unshifted reference collected

simultaneously. To ensure that the measured frequency shift is due solely to the Doppler effect, and not pressure or temperature differences, this comparison should be done with a feature collected at the same conditions. This can be done by simultaneously measuring the absorption feature with a second beam perpendicular to the flow. Alternatively, larger frequency shifts and higher measurement accuracy may be obtained using two parallel laser lines propagating in opposite directions aligned with the flow. A schematic of this setup is shown in Figure 2.1 with corresponding example $2f$ signals shown in Figure 2.2

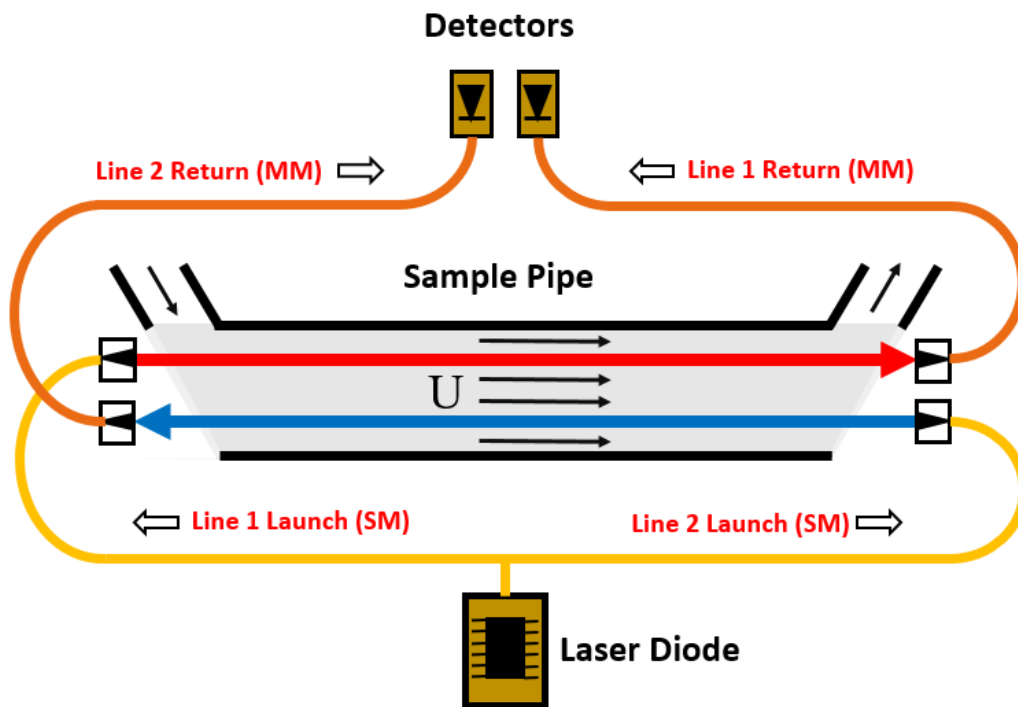


Figure 2.1: Schematic of the laser beam configuration used in OTEMS, simplified to only two lines. Line 1 propagates with the flow direction U while Line 2 counter propagates in the opposite direction. Both lines are launched and collected by collimators, before being sent over fiber optic to their respective detectors. Yellow launch fibers are single mode, while orange return fibers are multi mode. Flow direction is reversible.

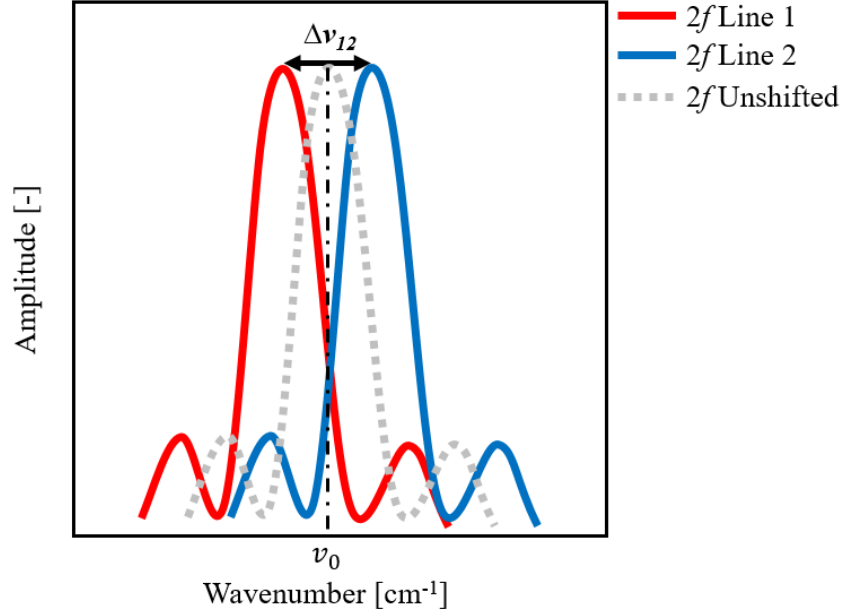


Figure 2.2: Idealized $2f$ signals from two counter propagating beams in a flow, demonstrating the Doppler shift in their absorption frequency. The unshifted feature is shown for reference as a dashed grey line.

The total shift between the two lines, Δv_{12} , is then related to the flow velocity by:

$$\Delta v_{12} = 2 \frac{v_0 U}{c} \quad (2.18)$$

For the absorption feature targeted in the present work (detailed in Section 2.3), a flow velocity U of 1 m/s will result in a Doppler shift Δv_{12} of $8.73 \times 10^{-5} \text{ cm}^{-1}$ ($5.1 \times 10^{-6} \text{ nm}$). This minuscule shift is less than 0.1% of the FWHM of the selected absorption feature. Accurately measuring such small shifts is the principal challenge of this work. In the presented OTEMS, four parallel laser beams aimed in opposite directions (two in each direction) are used, and the average Doppler shift is calculated through an innovative cross-correlation algorithm detailed in Section 3.9.2.1.

2.2.1 Review of Doppler Shift Velocity Measurements by TDLAS

The possibility of using the Doppler shift of absorption lines to measure the velocity of a flow field was first suggested by Measures (1968). Due to the state of spectroscopy at the time, the author believed that only a supersonic flow would yield sufficiently great of a Doppler shift to be measurable. Many of the experiments that followed this idea were thus conducted in supersonic flow fields. Table 2.1 presents an overview of the progression of techniques used to measure the velocity of a flow using absorption spectroscopy and the Doppler effect. Both line of sight absorption and fluorescence based techniques are included. Other optical techniques that have been used to measure flow velocities, such as transit time velocimetry (TTV) (Hiller et al., 1984; Sell, 1985; Zapka, 1982; Sontag and Tam, 1985; Rose and Gupta, 1985), photothermal deflection spectroscopy (PDS) (Dasch and Sell, 1986; Nie et al., 1986; Sell, 1984; Weimer and Dovichi, 1985), Raman spectroscopy (Moosmüller et al., 1984; She, 1983; Byer et al., 1981; Herring et al., 1981), and laser Doppler velocimetry (LDV) (Drain, 1980) are not included in Table 2.1. LDV requires seeding flows with particles to achieve a high enough return signal which is prohibitive since these seeding particles would contaminate the product kept in storage tanks. Raman spectroscopy methods often suffer from poor signal levels due to a reliance on a relatively weak scattering mechanism (Hiller and Hanson, 1988). Although both transit time velocimetry and photothermal deflection spectroscopy can measure low velocities, neither is well suited to measurements of liquid storage tank venting. TTV measures the velocity of a flow by tagging a volume of gas (e.g. laser illumination of phosphorescent seed particles injected into the flow (Hiller et al., 1984) or injection of nitric oxide which can be excited by a high-power laser (Sánchez-González et al., 2011)) which can subsequently be detected at a downstream location. The requirement for flow seeding and/or high power lasers makes this approach infeasible for

hydrocarbon storage tanks application. In addition, TTV techniques are unable to produce concurrent concentration measurements. PDS uses a high-power heating beam to induce local thermal gradients and hence local changes in refractive index. A second probe beam is aimed at a position sensitive detector. These two beams can be used in two distinct configurations. The first configuration, which could also be classified as a TTV technique, places the probe beam downstream of the heating beam. Deflections in the probe beam measured by the position sensitive detector are used to detect the arrival of the locally heated gas, and the transit time is used to calculate the flow velocity (Sell, 1985). In the second configuration the heating beam and the probe beam intersect at right angles at the desired measurement location in the flow. This alternate method relies on the heated gas taking on the same profile as the heating beam's power density profile. Any velocity in the flow will thus distort the profile of the induced index of refraction profile, which will in turn vary the deflection of the probe beam proportionally to the flow velocity as it traverses the heated region (Nie et al., 1986). While in principle it is possible to use the measured velocity and probe beam deflection amplitude to measure concentration of the absorbing species (Sell, 1985), it is unclear whether this approach would be suitable in a stream of hydrocarbon vapours with unknown and variable mixture properties. Moreover, the use of lasers with sufficient power to heat the gas flow is undesirable in hydrocarbon storage tank applications due to ignition concerns.

Table 2.1: Performance of TDLAS Velocity Systems

Reference	Detection Technique	Application	Target Species	Target Wavenumber [cm ⁻¹]	Optical Path Length	Absorption	Velocity Range	Velocity Precision
(Cattolica et al., 1978)	Fluorescence at multiple discrete wavelengths ¹	Supersonic Jet	9.5% Ne in He; 10.1% Ar in He; and 10.1% Ne, 9.8% Ar in He	He: 19937.52 Ne: 17088.17 Ar: 21693.86	0.00635 m	N/A	1154 or 1262 m/s	N/A
(Miles et al., 1978)	Fluorescence via SI	Supersonic Jet	Sodium at 233 K and 9 Torr seeded into flow	16977.9	N/A	N/A	~ 300 – 2100 m/s	~±70 m/s
(Zimmermann and Miles, 1980)	Fluorescence via SI	Hypersonic Jet	Sodium at 295 K and 1550 kPa seeded into flow	16977.9	N/A	N/A	Mach 11	Accuracy ±2 m/s
(McDaniel et al., 1983)	Fluorescence at multiple discrete wavelengths ²	Supersonic Nozzle	Iodine seeded into flow	19436.3	Planar	N/A	652 - 718 m/s	2% FS, Accuracy ±5 m/s
(Hiller et al., 1983)	Fluorescence at a single wavelength ³	Subsonic Jet	Iodine at room temperature and 50 to 200 Torr seeded into flow	18270.5	Planar	N/A	5-50 m/s	Accuracy ±10%
(Cheng et al., 1983)	Fluorescence via SI	Supersonic Jet	Sodium at 100-350 K and 12 Torr seeded into flow	16977.9	N/A	N/A	Mach 3.4	Accuracy ±0.2 Mach
(Hiller and Hanson, 1988)	Fluorescence at a single wavelength ³	Supersonic Jet	Iodine at 200-290 K and 90-180 Torr seeded into flow	19436.3	N/A	N/A	430 m/s	Error ~8%
(Paul et al., 1989)	Pulsed Planar Imaging of Fluorescence	Supersonic Jet	NO at 5 Torr seeded into flow	44202.0	Planar	N/A	Mach 2-7.2	Error <10%
(Chang et al., 1990)	Fluorescence via SI	Supersonic Jet	OH at 1000-1400 K and 0.5-1.5 atm	32625	N/A	N/A	900 – 1300 m/s	±50 m/s
(Davidson et al., 1991)	Multiple ⁴	Shock Tube	OH at 1100-3300 K and 0.1-0.8 atm	32625	16.5 cm ⁷	N/A	700 – 1400 m/s	Method 1: ±1% Method 2: ±5% Method 3: SD >100 m/s

Table 2.1: Performance of TDLAS Velocity Systems (continued)

Reference	Detection Technique	Application	Target Species	Target Wavenumber [cm ⁻¹]	Optical Path Length	Absorption	Velocity Range	Velocity Precision
(Chang et al., 1991)	SI	Shock Tube	NO at 800-2900 K and 0.2-1.2 atm	44444.4	16.5 cm ⁷	25-80 %	500 – 1300 m/s	N/A. Mentions ±30 m/s
(Philippe and Hanson, 1991)	WMS – 2f	Shock tube	O ₂ at 500-1100 K and 0.4-1 atm	13163.1	16.5 cm	Absorption 0.2 – 0.9 %	500 – 1000 m/s	±75 m/s
(Philippe and Hanson, 1993)	WMS – 2f	Shock Tube	O ₂ at 500-1100 K and 0.4-1 atm	13153.4	16.5 cm	Absorption 0.2 – 1.0 %	500 – 1000 m/s	±50 m/s
(Arroyo et al., 1994)	SI	Shock Tube	A: H ₂ O at 950-1200 K and 0.02-0.08 atm B: H ₂ O in O ₂ at 460-950 K and 0.1-0.5 atm C: H ₂ O in O ₂ at 600-1100 K and 0.4-1.1 atm D: H ₂ in O ₂ at 950-1250 K and 0.4-0.7 atm	7212.9	16.5 cm	Absorption A: 3-30 % B: 5-15 % C: 7-25 % D: 3-6 %	A:1350 - 1700 m/s B: 300- 900 m/s C: 550- 1100 m/s D: 950- 1200 m/s	±25 m/s
(Allen et al., 1994)	Fluorescence at a single wavelength ⁵	Supersonic Exhaust	OH at 1700-2400 K and 1 atm flame	35267	N/A	N/A	400 – 2000 m/s	±50 m/s
(Miller et al., 1996)	SI	A: Wind Tunnel B: Turbine Inlet	O ₂ in ambient air	13086.1 and 13078.2	A: 0.15 m B: 0.92 m	A: 0.24 % B: 1.7 % ⁸	A: 0-120 m/s B: 0-150 m/s	A: 2σ = 10 m/s B: 2σ < 1 m/s
(Miller et al., 1998)	SI	Indoor Enclosure	O ₂ in ambient air	~13100	1 m	2-2.3% ⁸	Quiescent	σ=3.5 m/s
(Upschulte et al., 1999)	SI	Scramjet Combustor	H ₂ O at 944, 1111 or 1250 K and either 6 or 12 psia	7605.8-7632.1	18 cm	N/A	970- 1130 m/s	±100 m/s
(Lyle, Jeffries, and Hanson, 2007)	WMS – 2f & SI	Wind Tunnel	O ₂ in ambient air	13084.2	108 cm	2.8 % ⁸	0-23 m/s	1 s SD = 0.22 m/s
(Lyle, Jeffries, Hanson, et al., 2007)	WMS – 2f & SI	Turbine Inlet	O ₂ in ambient air	13084.2	150.5 cm	3.5 %	25-175 m/s	1 s SD = 5.4 m/s

Table 2.1: Performance of TDLAS Velocity Systems (*continued*)

Reference	Detection Technique	Application	Target Species	Target Wavenumber [cm ⁻¹]	Optical Path Length	Absorption	Velocity Range	Velocity Precision
(Chang et al., 2010)	WMS – $2f/1f$ ⁶	Wind Tunnel	H ₂ O in ambient air (1 % mole fraction)	7294.1	184 cm	89% ⁸	2.5-18 m/s	±0.5 m/s
(Chang et al., 2011)	WMS – $2f/1f$	Supersonic Nozzle	H ₂ O at 714-935 K and 72 kPa	7454.34 and 7412.9	18.7 cm	25% ^a	1440-1630 m/s	$\sigma=14$ m/s
(Schultz et al., 2014)	WMS – $2f/1f$ & SI	Scramjet Combustor	H ₂ O at 800-2000 K	7185.6 and 6806.0	N/A	3.4%	500-1070 m/s	$\sigma=11$ m/s
(Strand and Hanson, 2015)	WMS – $2f/1f$	Scramjet Combustor	H ₂ O at 1119 K and 40 kPa	7185.60 and 7444.36	106 mm	12% ⁸	1885 m/s	SD ±26 m/s

¹ 3 wavelengths were used, one located at the line centre of the absorption feature and one each to the left and right.

² 23 discrete frequencies were used, each spaced by 150 MHz, to resolve the full absorption feature

³ A single frequency was used, which was located on the wing of the absorption profile. The difference in detected fluorescence between a red-shifted and a blue-shifted line was used to calculate the Doppler shift.

⁴ Method one: Time of flight. Done by marking a volume of gas by electrolysis (creation of OH) and subsequent detection by absorption of this OH further down the shock tube. Method two: Sweep integration (called wavelength modulation spectroscopy by the authors). Method three: DA (called fixed-frequency by the authors). Changes in absorption in a Doppler shifted and a non-Doppler shifted line were compared. These lines were at an off-resonance frequency.

⁵ Two counter-propagating sheets of laser light were used. The ratio of the fluorescence in the two sheets is used to measure velocity.

⁶ WMS $2f/1f$ normalizes the $2f$ signal by the first harmonic, $1f$, to reduce vibrational and beam steering noise.

⁷ Path length inferred from subsequent studies using the same or similar shock tube apparatus

⁸ Estimated using given test parameters from the HITRAN2008 database (Rothman et al., 2009)

McDaniel et al. (1983) seeded a supersonic nitrogen flow field with iodine and used an argon-ion laser to detect the absorption with fluorescence detection. The absorption lines of interest were the P13 and R15 lines in the (43-0) band of the B-X system of iodine, at 514.5 nm. They achieved a velocity accurate to ± 5 m/s with an uncertainty of 2% of full scale at Mach 3.3 to 5.0. This accuracy was limited by the linewidth of the iodine absorption feature, which benefitted from being narrowed at the low pressure and temperature observed in the supersonic flow. In their conclusion, they suggested that a similar approach could be used for lower velocity regimes. In subsequent work, the argon-ion laser has its frequency centered on a wing of the R63 absorption line in the (25-0) band of the B-X system of iodine, at 547.33 nm. The frequency shift was found by estimating a linear slope for the absorption line at the scanned wavelength. This technique was applied to velocities from 5 to 50 m/s (Hiller et al., 1983).

Chang et al. (1991) used a continuous wave (cw) laser to measure velocity, along with temperature and pressure, in 1-D high velocity shock tubes. The use of a cw laser allowed for the full resolution of their target absorption features, which were a pair of lines in the absorption spectrum of nitrous oxide around 225 nm. This was among the first experiments involving a naturally occurring absorption line, thus not requiring any seeding. The procedure used to determine the peak shift required an iterative fitting of Voigt profiles.

Philippe and Hanson (1991; 1993) used commercially available diode lasers capable of operating at frequencies corresponding with absorption lines of oxygen near 760 nm to measure velocity and density in shock tubes. This set of experiments also introduced wavelength modulation techniques and second harmonic detection. The central portion of the $2f$ peaks were fitted using a second (1991) or fifth-order (1993) polynomial to determine the frequency shift $\Delta\nu$.

The results of Phillippe and Hanson generated interest in using their technique to measure the air mass-flux in turbine engine inlets. The potential for an onboard sensor made this an attractive idea. Miller et al. (1996) used a fiber-coupled AlGaAs Fabry-Perot diode laser to probe two oxygen absorption lines, located at 764.2 nm and 764.6 nm. Despite the low absorption strength, the continuous and significant concentration of oxygen in the turbine air flow ensured a reliable detection. The output of the diode was coupled into 60 m fibers to allow for a remote measurement. Two measurement schemes were investigated: the first involved recoupling the light into 100 μm core multimode fiber optic cables, the second directed the collimated beam directly onto a detector with a 6 mm square Si diode surface area. Vibrations and beam steering led to the first method being deemed unsuitable for field measurements. Three methods of determining frequency shifts used to calculate flow velocity were described: a FWHM method, a derivative method, and a Voigt method. All methods were applied to a sweep integration result. Tests were conducted on a Pratt and Whitney F-100 turbine engine. A zero-velocity offset was observed in quiescent conditions and subtracted from all results, indicating a test specific calibration was required. The Voigt method of determining the velocity yielded the lowest standard deviation, as low as 0.40 m/s when the light was captured directly onto the detectors. The precision of the velocity measurement dominated the precision of the mass flux measurement. No quantified uncertainty was given for the optical re-coupling scheme (Miller et al., 1996).

Following the relative success of this turbine engine mass flux sensor, Lyle, Jeffries, and Hanson (2007) integrated WMS techniques in an effort to improve the precision of the sensor. A low velocity wind tunnel was used to verify the subsonic performance of a mass flux device based on oxygen absorption near 764 nm. This wind tunnel test used a fibre-coupled vertical-

cavity surface-emitting laser (VCSEL). Alternating density and velocity measurements were made to collect mass flux data. Density measurements were based on an SI method, while velocity measurements are made using WMS. Each technique was done sequentially at a rate of 50 Hz. A 1 s standard deviation of 0.22 m/s was achieved for velocities up to 23 m/s. Further tests were conducted using the same general apparatus on a Pratt and Whitney turbofan, model PW6000. Due to the harsh environment, the VCSEL was replaced with a fiber-pigtailed distributed feedback (DFB) diode. This diode was 15 times more powerful. System capability was increased to process real-time mass flux results from a laser scan rate of 100 Hz, with 1 second averaging of the detector signals. Density and velocity measurements remained sequential. A 1 s standard deviation of 5.4 m/s was reported for all test velocities, and 1.85% for all test densities. Calculated mass flows had a 1 s standard deviation of 10.2 kg/s (Lyle, Jeffries, Hanson, et al., 2007).

2.3 Absorption Peak Selection

The OTEMS takes advantage of the presence of oxygen within the gas-vapour mixture which is exchanged between a tank's vapour space and its surroundings. When fresh air is ingested into the tank's vapour space it will cause some of the stored hydrocarbons to evaporate. If left undisturbed for long enough, saturation conditions will be reached. When the vapour space expands due to temperature changes or product is added to the tank, an equivalent volume of gas-vapour mixture is expelled to the atmosphere. The volume fraction of oxygen within this mixture relative to atmospheric conditions can be used to calculate the fraction of hydrocarbon vapours in the vented gas as shown in equation (2.19),

$$x_{vapour} = \frac{x_{O_2,\infty} - x_{O_2,V}}{x_{O_2,\infty}} \quad (2.19)$$

where x_{vapour} is the mole fraction of hydrocarbon vapours [%], $x_{O_2,\infty}$ is the mole fraction of oxygen in the ambient air [%], and $x_{O_2,V}$ is the measured mole fraction of oxygen in the tank vent line [%]. Equation (2.19) assumes that the only source of oxygen within the tank vapour mixture is from atmospheric air previously ingested into the tank, and that the ratio of oxygen to nitrogen in the ambient air is fixed. A previous study on an underground gasoline tank indicated that oxygen volume fractions as low as 10% can be expected in the gas-vapour mixture vented from the tank (Picard and Johnson, 2011). By combining an oxygen concentration measurement with a velocity measurement, a volumetric flux of emissions from the storage tank can be made. If it is desired to provide mass flux data on individual species, additional information of the composition of the hydrocarbons within the vapour is required. This can be achieved through a sample bagging protocol. Such a practice is fairly common within the oil and gas industry and can be done following established standards.

2.3.1 Absorption by O₂ and other interfering species near 764 nm

Oxygen was selected as the target species due to the relative isolation of its absorption in the lower ranges of the near-IR, specifically around 764 nm. The non-reliance on a specific hydrocarbon absorption peak allows the OTEMS to be used in a wide variety of situations, since under normal operating conditions fixed-roof storage tanks will always breathe in atmospheric oxygen. Figure 2.3 shows the absorbance for the most common atmospheric gases from 762.8 nm to 764.8 nm (13075 cm⁻¹ to 13110 cm⁻¹) at 25°C, 1 bar, and a path length of 1.57 m calculated from the HITRAN2008 database (Rothman et al., 2009).

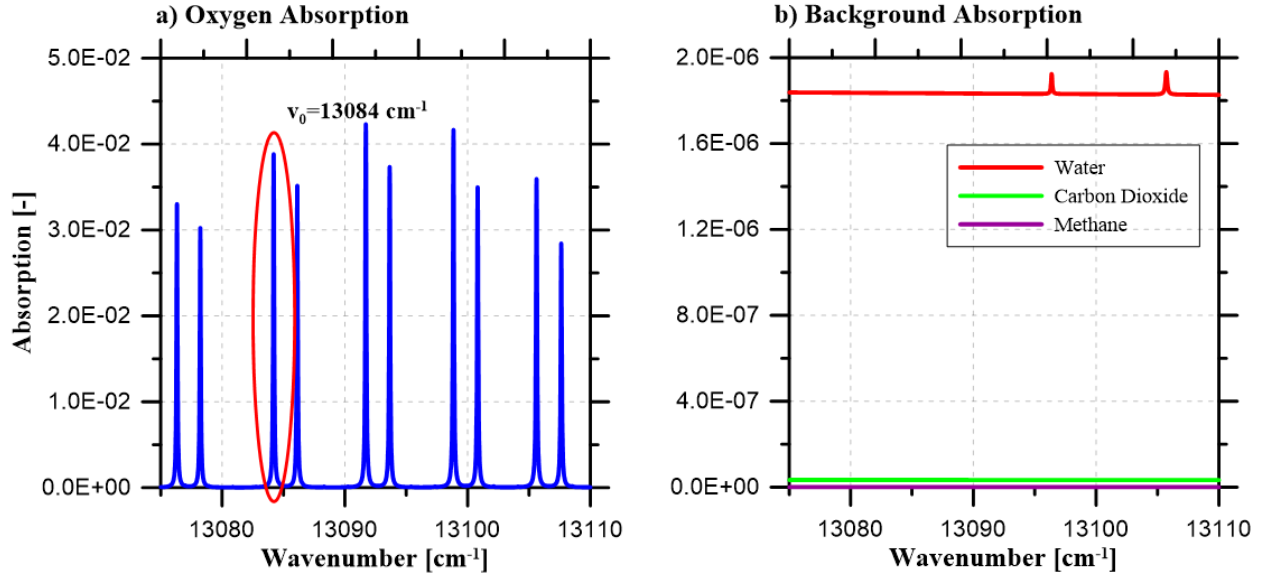


Figure 2.3: a) Absorption of oxygen from 13075 to 13110 cm⁻¹ at 21% concentration. 25°C, 1 bar, and a path length of 1.57 m, target absorption line for OTEMS circled in red at a center frequency of 13084.21 cm⁻¹. b) Absorption of common atmospheric gases (water 31690 ppm, carbon dioxide 400 ppm, and methane 2 ppm) from 13075 to 13110 cm⁻¹ at 25°C, 1 bar, and a path length of 1.57 m.

As can be seen in Figure 2.3, oxygen has multiple absorption peaks that are isolated from themselves and from other common atmospheric gases. Comparable absorption strengths of water, CO₂, and CH₄ at expected maximum concentrations of 31690 ppm, 400 ppm, and 2 ppm are at least 20000 times less than that of O₂ at 25°C and 1 bar. The absorption peak that was selected for OTEMS is at 13084.21 cm⁻¹. It was selected over its neighboring peaks for the ease at which it could be targeted by the laser diode used within OTEMS. Since this is not a region of the near-IR commonly utilized within telecommunications technologies, there is a noticeable difficulty in sourcing appropriate hardware. The selection of laser diodes near 764 nm was therefore limited. This wavelength also dictates many of the fiber-optic components that are described in Chapter 3.

Chapter 3 Experimental Setup

3.1 General Description

The TDLAS apparatus can be separated into two main components. As shown in Figure 3.1, these are the base tower (which includes the host computer, field programmable gate array (FPGA) and associated data acquisition system, laser controllers and mounts, power supplies, and thermo-electric cooler box) and the remotely locatable sample pipe. Components in the base tower are mounted in three Pelican™ cases with Hardigg™ mounting rails. These cases are stacked vertically to minimize their footprint. They can easily be closed for shipping, and care was taken to minimize connections required between the cases to expedite field setup. The sample pipe sensor consists of an open ended pipe section through which the tank vent gases would flow, along with the required optical elements. Fiber optic cables and, depending on the configuration, co-axial analog signal cables connect the base tower to the sample pipe. The components of the OTEMS are discussed in detail in the sections that follow.

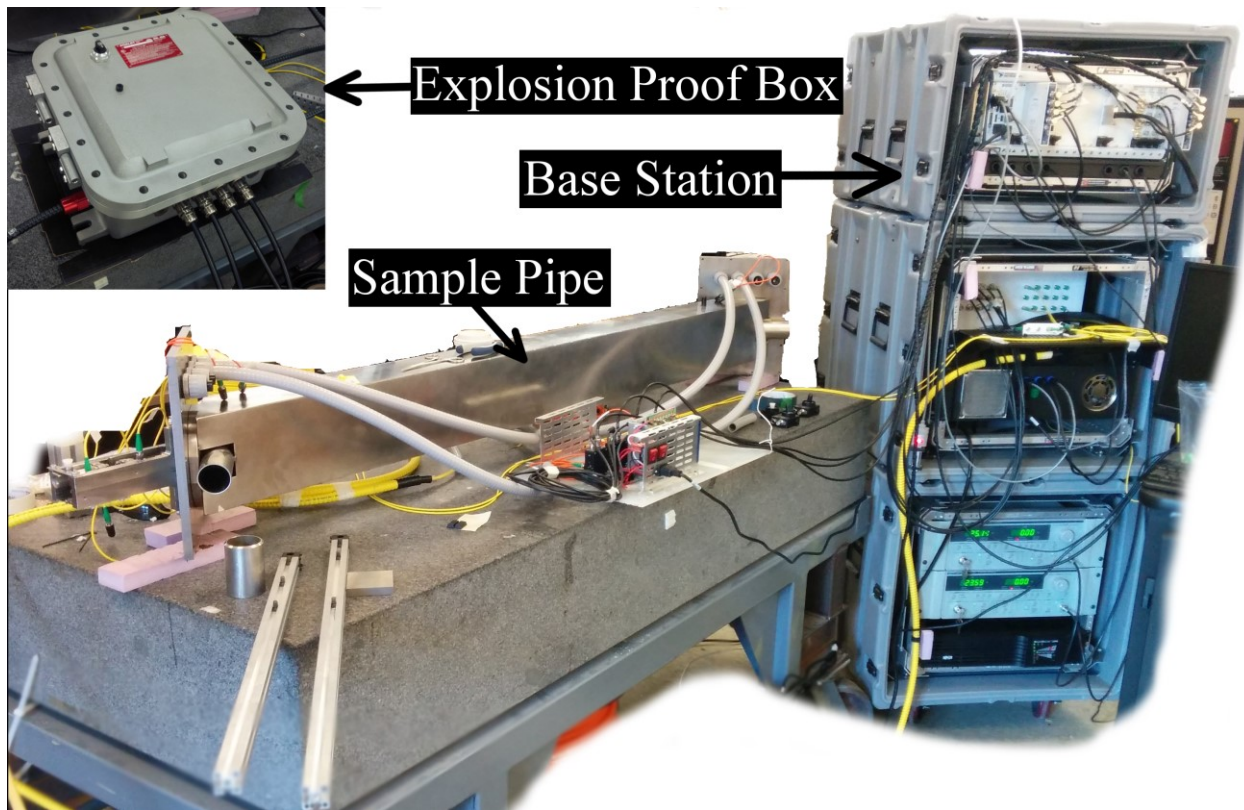


Figure 3.1: Photograph of the complete OTEMS in an earlier stage of development. The three Pelican™ cases on the right are the base station, while the metal structure on the granite table is the sample pipe. Note that the end caps are not installed. The explosion proof box, detailed in Section 3.6.7, is included in the upper left corner. The contents of this box are seen in front of the sample pipe on the granite table.

3.2 Laser Diode

The TDLAS system uses a distributed feedback (DFB) laser diode. DFB lasers are compact in size and output an extremely narrow linewidth; a typical half width at half maximum (HWHM) is 0.003 cm^{-1} or 1 MHz. This latter feature makes them well suited for gas sensing applications as they can accurately resolve individual absorption features. For comparison, at room temperature and pressure the HWHM of the O_2 absorption feature targeted by the OTEMS is 0.048 cm^{-1} or 2.9 GHz. As detailed in Saleh and Teich (2007), the narrow linewidth of DFB lasers is produced by a diffraction grating which only permits a certain wavelength of light to escape the diode. In the same fashion as other laser diodes, the DFB laser is a forward-biased p-n junction with a direct band gap semiconductor material. It is this direct band gap which allows

for photon emission through electron-hole recombination. Lasing is achieved by driving the laser diode with a current above the threshold injection current. Once this current is reached, optical amplification exceeds any losses in the optical cavity and the diode will begin to emit light. The center wavelength of the light output by the diode can be varied through either temperature tuning or current tuning. Both of these methods slightly alter the pitch of the diffraction grating by altering its refractive index through thermal expansion, which in turn affects the wavelength of light selected by the grating (Saleh and Teich, 2007b).

The laser diode chosen for this system was manufactured by eagleyard Photonics (Model EYP-DFB-0764-00010-1500-BFY02-0002) and was supplied in a 14-pin butterfly mount with a built in thermo-electric cooler/heater (TEC). The laser output was fiber coupled into single mode polarization-maintaining 5/125 fiber with an FC/APC connector. The output power was approximately 10 mW.

3.3 Laser Controller

The laser diode was mounted into an ILX Lightwave diode mount (model LDM-4980) which was combined with an ILX Lightwave controller (model LDC-3724C). This controller regulates the temperature of the diode through its built in TEC, and also controls the current tuning of the diode. The laser controller can be adjusted either through a front panel or through a USB interface via the host computer. An external modulation input provides the controller with a varying voltage signal that is used to modulate laser current. The low frequency sweep and high frequency modulation are combined using a bias-tee and sent to the controller through this input. These signals originate from frequency generators in the host computer, as further detailed in Section 3.8.3.

3.4 Photodetectors

Silicon semiconductor photodetectors (Thorlabs model PDA36A) with a 3.6mm square detector surface were used. These detectors include an integrated transimpedance amplifier with user selectable gain, mounted within a compact housing. The detector responsivity is approximately 0.5 A/W at 760 nm. These detectors were selected due to their relatively large semiconductor surface area. This large area allows for a stable return intensity when used in conjunction with a 2 mm collimated beam. These same detectors were used in the design of the sensor when a fiber re-coupling scheme was adopted. Fiber adapter plates (Thorlabs model SM1FCA) were used to attach the fibers containing the re-coupled light directly to the detectors. These adapter plates butt couple the fiber directly in front of the detector diode. Since the large detector surface area is no longer required in such a situation, an alternative detector with a faster response and lower noise could improve system performance. This option was not investigated for the first version of the field deployable unit as a cost saving measure. In total, the OTEMS uses seven of these photodetectors – three in the thermally stabilized enclosure (Section 3.5.4) and four in an explosion-proof box (Section 3.6.7) located near the sample pipe.

3.5 Optical Setup

3.5.1 Single Mode Fiber & Splitters

The light output from the laser diode, once coupled into a fiber optic cable, must be divided into multiple lines so that simultaneous measurements may be taken from various points in the system. A diagram of the fiber optic splitter network is presented in Figure 3.2. Fiber optic taps were used to split off portions of the laser light as required for various components. These taps and components were fused together into a single optical network to minimize losses introduced

by connectors. The network was connected to the laser's output fiber via a single FC/APC connector. Single-mode fibers (OZ Optics, 4/125 fiber) were used to deliver the light to the sample pipe. This ensured that losses due to light escaping into the cladding of the fiber were minimized.

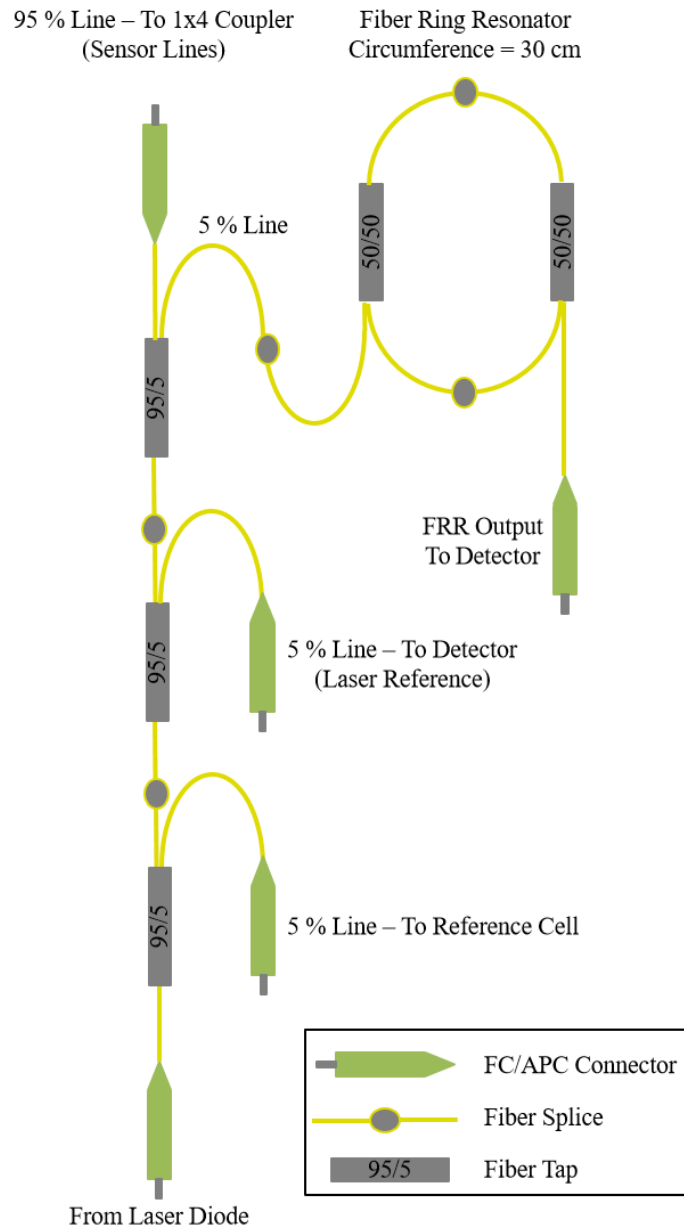


Figure 3.2: Diagram of fiber optic network used to tap optical power from the laser diode for the reference cell, laser reference, and fiber ring resonator (also shown in diagram)

Many of the components in the fiber optic network rely on single mode operation. These include the splitters and the fiber ring resonator (FRR). Limiting the light propagation to a single mode also removes the potential for modal dispersion, which occurs when the light can travel down the fiber in more than one mode. Since each mode travels a slightly different length, light from each mode arrives at the output end at different times (Saleh and Teich, 2007b).

The output line of the fiber network was connected via an FC/APC connector to a 1×4 25/25/25/25 output coupler. This coupler created the four main sample lines which were used for the mass flux measurement. The coupler was not fused to the network to allow for different output configurations. Since the fiber optic taps and couplers were sensitive to temperature changes, they were located within a temperature stabilized enclosure (further detailed in Section 3.5.4). The couplers and their associated fiber were also supplied by OZ Optics, using the same single mode 4/125 fiber so as to maintain consistency and minimize fiber mismatch losses.

3.5.2 Fiber Ring Resonator

The fiber network includes a fiber ring resonator (FRR), built from two 50/50 couplers connected as shown in Figure 3.2. The input line is fused to the 5% line of a 95/5 coupler, and the output line leads directly to a photodetector. The output of a FRR is an interference pattern based on the wavelength of input light (Urquhart, 1987b). It is important to note that the FRR does not allow for an absolute wavelength measurement. However, the interference pattern generated by a FRR can be used to accurately measure relative changes in wavelength in time, since the distance between interference peaks corresponds to a known wavelength change. This wavelength change is defined by the free spectral range (FSR) of the FRR, which is determined by the length of fiber creating the ring between the two couplers (L_{FRR}) and the effective

refractive index of the fiber used (n_e). Adapted from Urquhart (1987), equation (3.1) relates these quantities with the speed of light c .

$$\Delta\nu (FSR) = \frac{c}{2n_e L_{FRR}} \quad (3.1)$$

The FRR length was chosen so that an adequate number of interference peaks would be present when the laser was driven to scan the absorption feature of interest. However, since the FRR used in this system was constructed by a third party using relatively inaccurate splices, the FSR was not known a priori. Instead, the FSR was measured via a large sweep amplitude (a_{sweep}) WMS experiment. By scanning a wide enough wavenumber range to capture two identifiable neighboring oxygen peaks, the number of interference fringes in the FRR could be used in conjunction with the known wavenumber distance between the oxygen absorption peaks to calculate the FSR of the FRR. The eagleyard diode used in the OTEMS was unable to capture two absorption features due to its limited wavelength tuning range. Solely for the purpose of calibrating the FRR, a nanoplus diode (model DFB-076083 with mounting option MNT-350-SM) was used, which had a much larger wavelength tuning range. This diode had a lower power output than the eagleyard diode and was therefore not selected for use in the main system. An example signal from the FRR is included in Section 3.9.1.1.

3.5.3 Oxygen Reference Cell

One of the 95/5 taps in the fiber optic network was connected to an oxygen reference cell. The 5% fiber from this tap was connected to a reflective collimator (Thorlabs, model RC02APC-P01), which was mounted within a 25 mm cage system. Also mounted within the cage system

was a 20 cm long cylindrical quartz tube filled with pure oxygen at 740 Torr, with anti-reflective (AR) coatings on both end windows. This is the oxygen reference cell, manufactured by Wavelength References, Inc. At the other end of the reference cell, a PDA36A photodetector was mounted. The collimated light from the reflective collimator travels through the quartz tube and directly irradiates the detector surface. This configuration was used to produce a reliable and constant $2f$ signal from the oxygen within the reference cell. This signal was used to ensure that the light from the laser diode remained centered on the oxygen absorption feature. An automatic process within the data acquisition system located the peak of the reference signal and adjusted the DC current to the diode accordingly. This process ensured that this re-centering process was independent of the oxygen concentration within the sample pipe.

3.5.4 Thermal Stability

Many of the components within the OTEMS are sensitive to temperature changes. The fiber optic splitters mentioned above are one example, as well as the oxygen reference cell and the laser diode mount. These components were placed within an insulated box whose temperature was stabilized using thermoelectric heater/cooler (TE Technology CP-200). To minimize fiber connections, the photo-detectors for the FRR, laser reference line and oxygen reference cell were also placed within the temperature stabilized box. To ensure proper convective circulation and avoid thermal stratification, all heat generating components were placed at the bottom of the box, with the cold plate of the thermo-electric cooler located at the top.

3.5.5 Launch – Fibers & Collimators

The laser light was carried from the 1x4 splitter within the thermally stabilized box to the sample pipe via four 75 m long single mode fibers. These fibers were jacketed with a 3 mm plastic coating for basic protection. In a field study application, these fibers should be armored and

combined within a single assembly. This armouring would preserve the integrity of the fibers during installation when routing them from the base station to the sample pipe. For the purpose of indoor calibration and prototyping, non-armored cables were used. At the sample pipe, the fibers were connected to reflective collimators (Thorlabs, RC04APC-P01) placed in pairs at opposite ends of the sample pipe. These collimators focused the laser light into beams of 4 mm diameter, which traversed the length of the sample pipe. Two of the beams travelled in one direction, and the other two travelled in the opposite direction. This created four pairs of beams which could be used to measure a velocity induced Doppler shift. The collimators were fixed in small 0.5” kinematic mounts (Thorlabs, POLARIS-K05S2), which could be adjusted with two set screws to direct the beam in two independent directions. Their small size allowed for a compact design, reducing the required diameter of the sample pipe. The mounts were designed using materials with matching coefficients of thermal expansion to maximize stability. A photograph of the collimators and their mounts can be found in Section 3.6.5.

3.5.6 Receive – Fibers, Collimators & Detectors

An earlier prototype of the vent flux measurement device placed detectors at each end of the sample pipe, such that the beams directly irradiated them. This design was less desirable for a field unit as the end of the sample pipe is designated as Class I, Zone 0 under the CSA system for hazardous locations. Strict regulations limit all powered electronics in a Zone 0 area to intrinsically safe units. The challenge of having the detectors approved for Zone 0 operation was deemed unreasonable due to a lack of pre-certified solution. For these reasons, the two beams were instead re-coupled into fiber optic cables to bring the light out of the Zone 0 area. The detectors were mounted within an explosion-proof enclosure that could be located in a Zone 1 or higher area. This enclosure is further detailed in Section 3.6.7.

To minimize the losses incurred by re-coupling, various combinations of fiber optics and collimators were tested. The final solution was to use 2-mm diameter reflective collimators (Thorlabs, RC02APC-P01) with multi-mode (MM) 62.5 μm graded index core fiber (Fiber Instrument Sales, IA-2-7A-7A-M-7-FIS-6). The MM 62.5 fiber, with a core diameter of 62.5 μm , captured a greater portion of the beam intensity compared to single-mode fibers, which for the present wavelength of 764 nm, had core diameters near 5 μm . A similar recoupling strategy was used by Strand and Hanson (2015). The larger core diameter also allowed for a greater degree of beam misalignment. This would be particularly advantageous for the field-deployable sensor. Beam misalignment can occur due to temperature changes causing the apparatus to expand and contract. Mechanical disturbances can also affect the relative alignment of the collimators, especially during sensor installation. The capture fibers were bundled within two 7 m long indoor/outdoor armored cables (one for each end of the sample pipe) and directly attached to the detectors within the explosion-proof enclosure. It was determined experimentally that returning the MM 62.5 fibers all the way to the base station, potentially 100 m away, was unfeasible due to the relatively high losses in the multi-mode fiber. This limitation is what led to the implementation of the explosion-proof box for the detectors so that they could be located close to the sensor, but outside the Zone 0 area. The MM cables were fixed to both the explosion proof box and the sample pipe ends with cable glands that preserved the explosion proof rating.

3.6 OTEMS Remote Sample Pipe

3.6.1 Overview

The remote measurement pipe refers to all components of the OTEMS that are to be located in proximity to the storage tank to be measured. This includes the sample pipe through which the

vent gas is diverted, the valves and tubing to connect to the tank, the hardware and optics attached to the sample pipe, as well as the explosion proof detector box.

3.6.2 Sample pipe

The purpose of the sample pipe was to provide a sufficiently long section of straight pipe through which the laser light and vent gas can concurrently travel. The measurement section was a 1.75” outside diameter pipe made of an Iron-Nickel alloy steel, Invar™, with a wall thickness of 0.06”. It was composed of a straight section 1.6 m in length with two symmetrically arranged, 50 degree elbows at either end acting as an inlet and an exhaust. The elbows provided an efficient passage for the gas mixture to enter and exit the sample section. Figure 3.3 shows the complete sample pipe. Invar™ faceplates were welded onto each end of the straight section to allow for mounting of the endcaps that housed the optical components.

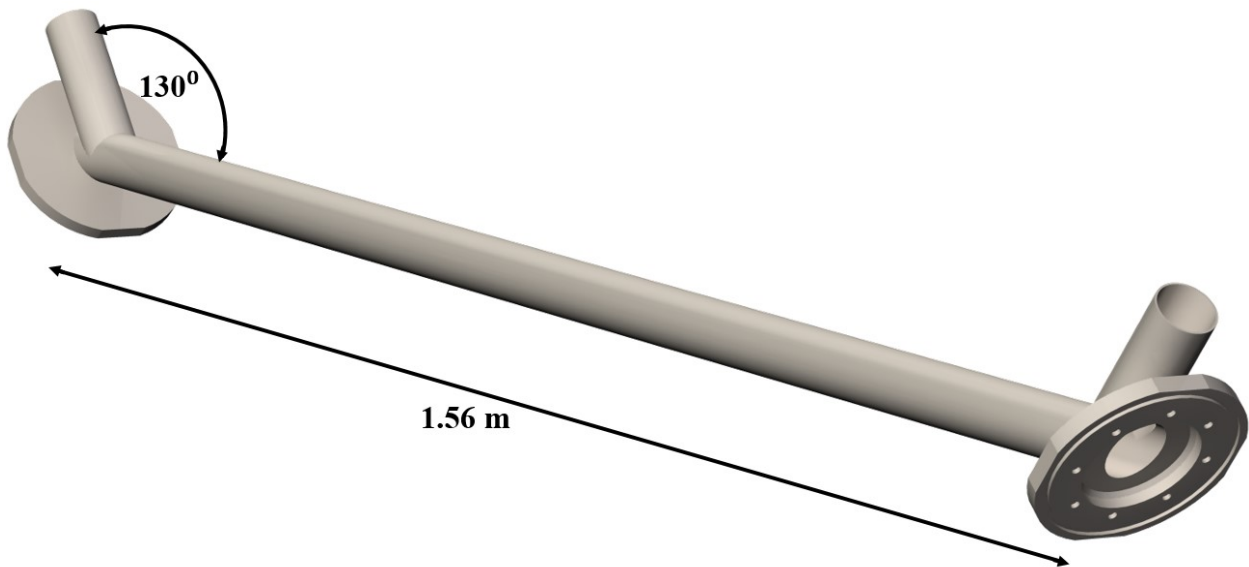


Figure 3.3: Render of the sample pipe with the inlet and outlet elbows and faceplates

The sample section was held inside an Invar™ steel box, which was welded to the faceplates. This provided added structural rigidity to minimize beam misalignment. The

complete sample section with its enclosure is shown in Figure 3.4. The holes at each end of the pipe allowed for the laser light to enter and exit through angled windows, which were sandwiched between the faceplate and the end cap mounting plates (see Section 3.6.3 for details).

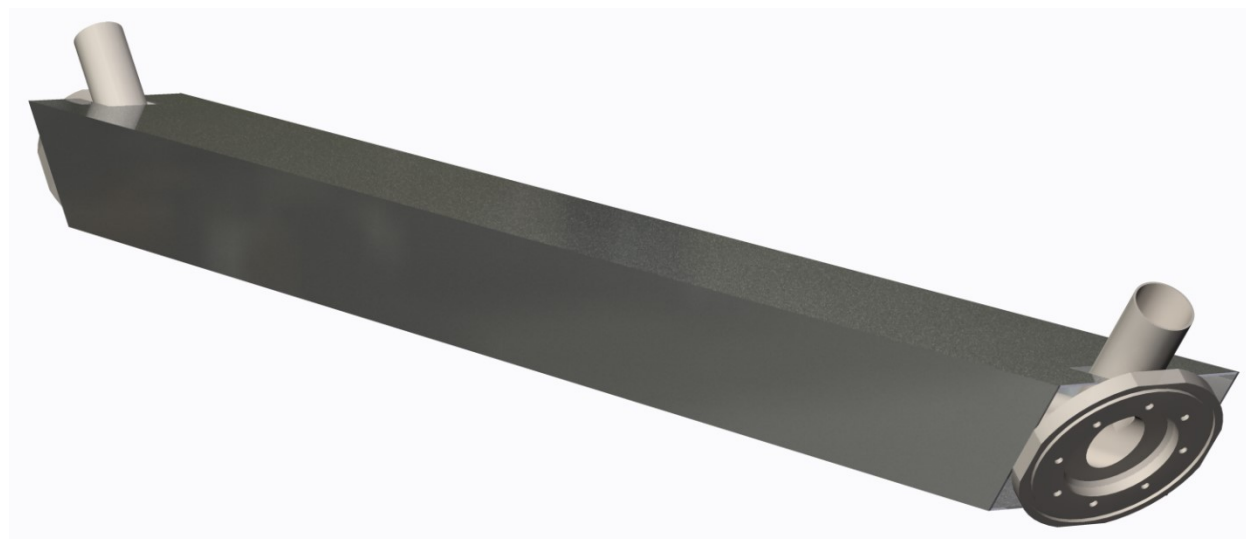


Figure 3.4: Render of the sample pipe with the welded box surrounding it

3.6.3 Windows

Located between the sample section and the end caps, $\frac{1}{4}$ " thick, 2.75" diameter windows provided an optical passage for the laser light into and out of the sample section. These windows were held in compression between the sample pipe faceplates and endcap mounting plates. A rubber gasket between the window and the sample pipe faceplate pushed the window against the endcap mounting plate and provided a seal. The windows were angled along with the sample section elbows, which prevented backreflections between the windows and collimators. The windows were also AR coated on both sides for 763 nm by BMV Optical Technologies.

3.6.4 End Caps

The end caps enclosed the optical components, including the launch and receive collimators, associated fibers, and connectors. The end caps were bolted to a mounting plate which in turn was bolted to the sample pipe faceplates. A gasket between the end caps and mounting plate provided a gas tight seal. The end caps themselves were made from bent and welded InvarTM sheetmetal sections, 0.06” thick. Entry into the end caps was possible through four 1” NPT and two ¼” NPT tapped holes in the mounting plate. These were used in the current OTEMS configuration for entry of the launch fibers, exit of the return multimode fibers, and inlet and exhaust for a nitrogen purging system. Purging the end caps with nitrogen minimized absorption from oxygen outside of the sample section. The nitrogen purge was regulated with a low pressure regulator (Equilibar, model 4116ANNKE-Z22006). The end enclosures were connected sequentially with ½” tubing, with the second enclosure being equipped with a check-valve to prevent over-pressurization. The photograph in Figure 3.5 shows a prototype of the end caps from a previous iteration of OTEMS. The clear plastic shows the space enclosed by the end caps, as well as the optics mounting platforms detailed in Section 3.6.5. Figure 3.6 shows the opposite end cap as described in this work. The single mode launch fibers in yellow and the armored capture MM fiber in black are visible, along with the nitrogen purging lines in white plastic.

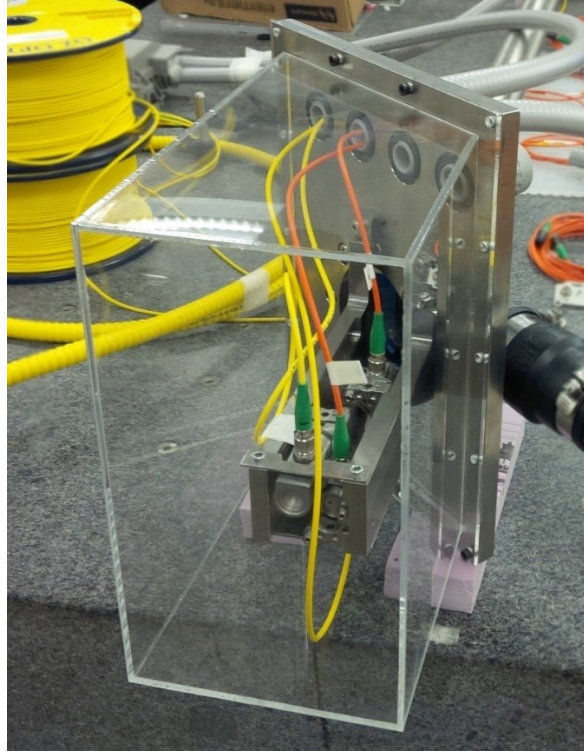


Figure 3.5: Early prototype of the end caps, manufactured with clear plastic. Visible through the plastic are single mode launch fibers in yellow and capture multimode fibers in orange.

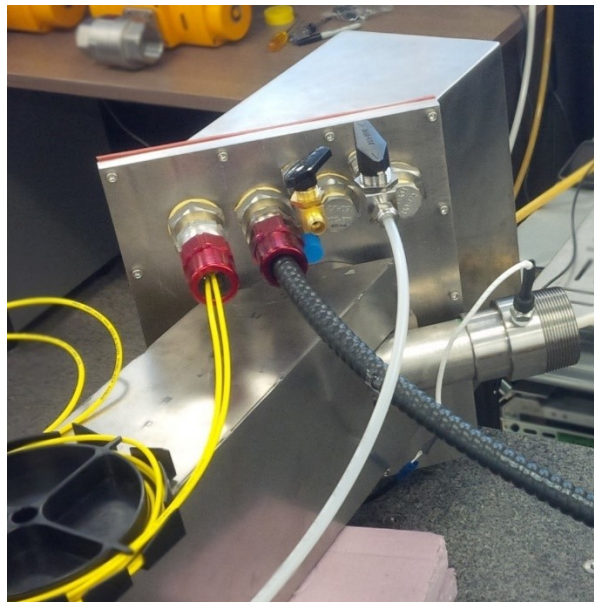


Figure 3.6: Photograph of one end of the sample pipe. The Invar™ end cap is visible behind its mounting plate. The two launch single mode fibers in yellow and the capture multi-mode fibers in black are attached to the mounting plate. The clear plastic tube is the nitrogen purging system, which vents through the gold valve.

3.6.5 Optics Mounting Platforms

The launch and receive collimators were mounted to Invar™ platforms. There were two optics platforms per end and these were bolted to the end cap mounting plates. These platforms provided a stable base for the collimator mounts while allowing access to the latter's adjustment screws for alignment. The two optics platforms at each end were held together with cross braces to minimize vibrations in the cantilever structure. Figure 3.7 is a photograph of the optics platforms with the launch and receive collimators from one end of the sampling pipe.

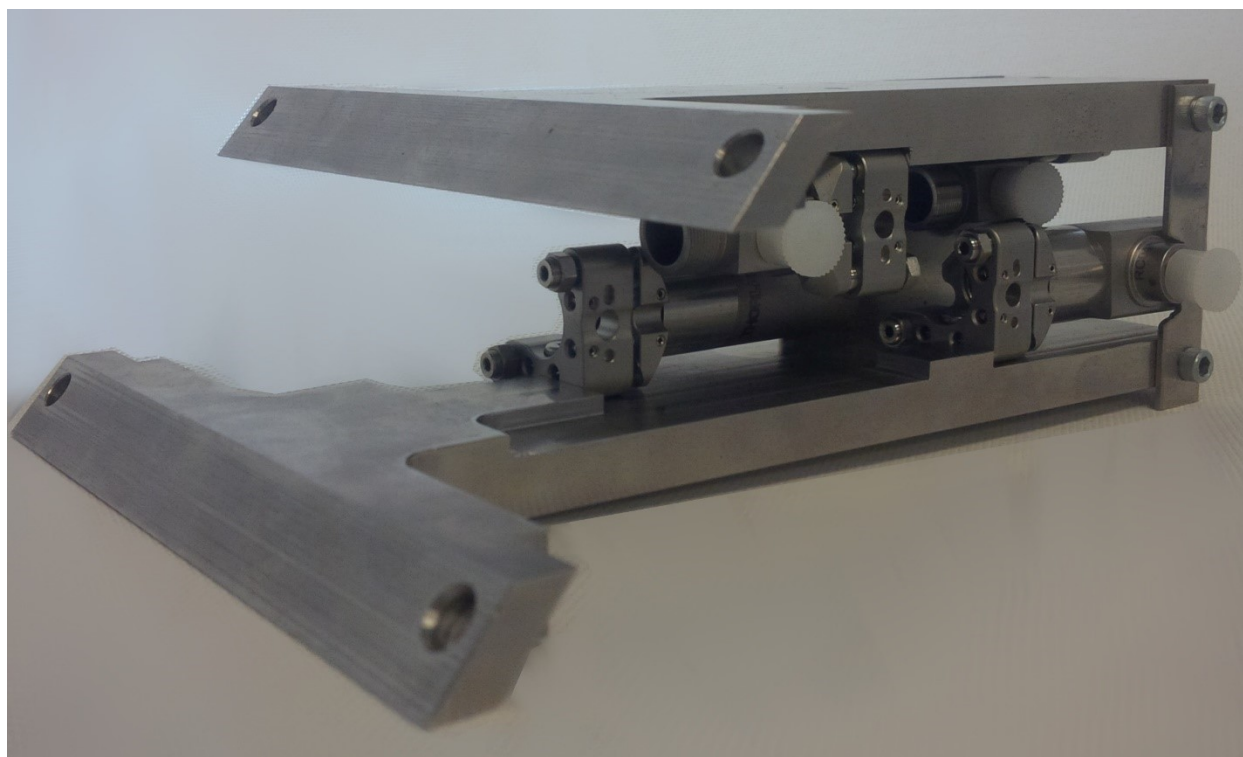


Figure 3.7: Photograph of the optics mounting platforms from one end of the sample pipe. The collimators, secured in their kinematic mounts, are shown. A stabilizing cross-brace is visible at the rear of the platforms.

3.6.6 Pressure and Temperature Sensors

As was described in Chapter 2, the $2f$ feature will vary with temperature and pressure due to broadening effects. Additionally, for calibration purposes the temperature and pressure inside the sample section are required to convert the standard litres per minute (calculated at 294.15 K,

101.325 kPa) reported by digital mass flow controllers (MFC) into actual litres per minute at ambient conditions. In the field the required pressure and temperature sensors will be specialty devices that are intrinsically safe and can be safely operated in a hazardous location. For the purpose of indoor testing and calibration, two Omega 44004 thermistors were used in combination with a digital pressure gauge (DPG) from Additel (model DT681). The pressure gauge and one thermistor were installed adjacent to the inlet elbow of the sample pipe, while the second thermistor was installed adjacent to the exit elbow. The average of the two thermistor readings and the pressure from the DPG were sampled at 1 Hz and incorporated into the velocity and concentration methodology presented in Sections 3.9.2 and 3.9.3.

3.6.7 Explosion Proof Box

Due to the strong intensity attenuation in multi-mode fibers, the length of the capture fibers was limited to less than 10 m. Thus, the four sample detectors needed to be located in close proximity to the sample pipe. The surroundings of the sample pipe are designated as a hazardous location with the potential for explosive vapours and any electronics must be certified to operate in such conditions. The detectors are therefore encased in an explosion proof box certified for use in a CSA Class I, Zone 1 area. This box was custom manufactured by Adalet from their XCE series of aluminum enclosures and includes ten ½” NPT tapped holes, one ¾-14 NPSM tapped hole, and one 3/8-16 tapped hole. The explosion proof box is shown in Figure 3.8.



Figure 3.8: Explosion proof box. Visible at the bottom are four LMR 400 cables, and to the left side is one multi-mode fiber optic cable (red cable gland). Box is shown not bolted shut.

These holes were used to feed all required cables and optical fibers into the box, or in the case of the 3/16” hole, to mount an indicator light. To minimize power losses, the current was sent to the explosion proof box over an AC power line. A DC power supply was securely placed within the box to provide the required power to the four detectors. A toggle switch mounted to the lid of the explosion-proof box controlled the AC power to the DC power supply. A time-delay relay was placed after the DC power supply to provide a delay between power-supply startup and the detectors receiving power. This prevented damage to the detectors from power transients that may be produced at startup. The detectors were connected to the base station DAQ through four, 77 m long, LMR400 co-axial cables. These cables have low signal attenuation over long distances.

3.7 Mass Flow Controllers

For the purpose of indoor calibration and validation, two digital mass flow controllers were used to mix compressed air and pure nitrogen to allow for the concentration of oxygen in the flow to be modified from 0 to 21% for flow velocities up to 3 m/s. Both mass flow controllers were Brooks model number SLAMF53S2DAB2F2A4, with a maximum output of 250 SLPM. These controllers were connected to the base station host computer which could set their output rates and read the returned rates. These rates were used as a reference value for both velocity and concentration in all results presented here. The returned rates were converted to actual LPM using the measured pressure from the DPG and the average of the inlet and outlet temperatures from the thermistors.

3.8 Data Acquisition

3.8.1 Host Computer – PXI Chassis

The heart of the base station is a National Instruments PXIe-1075 chassis paired with a PXIe-8135 controller. The PXIe-8135 has an Intel i7-3610QE quad-core processor, operating at 2.3 Ghz. It is equipped with 16 GB of random access memory and runs the Windows 7 operating system. All programming of the OTEMS was done through the LabVIEW programming environment. The PXIe-1075 allowed for the controller to interact with up to 18 PXI compatible expansion cards over a 4 GB/s backplane. The controller together with the expansion cards is referred to as the host computer. The tested configuration used two NI PXIe-7966R FlexRIO FPGA modules paired with NI 5734 Digitizer Adapter Modules, two NI PXI-5406 Arbitrary Function Generators, and a PXIe-6363 analog and digital IO car. These cards are further detailed below.

3.8.2 Field Programmable Gate Array (FPGA)

A key feature of the OTEMS is the use of field programmable gate arrays and associated digitizers as a data acquisition system. The NI PXIe-7966R FlexRIO contains a Xilinx Virtex-5 SX95T FPGA module. These modules can be programmed to perform various mathematical operations on their integrated circuits at very high speeds, which allowed for high sampling rates (120 MHz). Both FPGAs were paired with NI 5734 Digitizer Adapter Modules. These analog to digital converters were capable of sampling four channels simultaneously at 120 MHz. They were used in the OTEMS to acquire all detector signals: four sample lines, laser reference, fibre ring resonator, and reference cell. The FPGA used with the four samples lines was programmed to integrate the $2f$ signal in real time on all four lines. This calculation reduced the load on the host computer, which only received the $2f$ signal along with the average voltage for each modulation period. If the FPGA was programmed as a simple DAQ card with no data processing, the sample rate would have to be reduced to 20 MHz to allow time for the host computer to calculate the $2f$ signal. Such a sample rate would reduce the resolution across the $2f$ peak, reducing the ability to resolve a Doppler frequency shift. Since FPGAs are not well suited to perform square root operations, this final step of the $2f$ algorithm was left to the host computer. If $x_1(t_i)$ represents the detector voltage of sample line 1 at time t_i , then the FPGA calculated the squared $2f$ signal of sample line 1, $R_{2f_1}^2(t_j)$, as:

$$R_{2f_1}^2(t_j) = \frac{1}{M^2} \left[\left(\sum_{i=1}^M x_1(t_i) \cos(4\pi f_m t_i) \right)^2 + \left(\sum_{i=1}^M x_1(t_i) \sin(4\pi f_m t_i) \right)^2 \right] \quad (3.2)$$

where M is the total number of points in the modulation period. The second FPGA was configured to collect the detector signals of the fibre ring resonator, the laser reference, and the

oxygen reference cell. In the case of the reference cell, the FPGA calculated the squared $2f$ signal using equation (3.2) . Since the raw voltage from the FRR and laser reference was required, the FPGA simply sent this signal to the host computer after converting it to its digital equivalent. To maintain continuous data acquisition, the FPGA down-sampled these channels to 20MHz.

3.8.3 Frequency Generators

Two NI PXI-5406 Arbitrary Function Generators (FGEN) were used to modulate the laser diode. These cards produced a varying voltage which was converted into a varying current by the laser controller through its external modulation input. While one FGEN produced a triangle waveform for the sweep frequency, the second one produced a cosine waveform for the modulation frequency. The triangular sweep waveform varies the wavenumber of the laser so that it passes over the center of the absorption feature twice during a single sweep period. The first half of the sweep period, where the wavenumber is increasing, is referred to as the leading section of the sweep. The second half-period, where the wavenumber is decreasing, it referred to as the lagging section of the sweep. The waveform generation on both cards was synchronized using the backplane of the PXI chassis and its 10 MHz reference clock. The two waveforms were combined using a bias tee from Picosecond (model 5543). The amplitude and frequency of both the sweep and modulation could easily be varied by the FGENs, which allowed for a wide range of operational configurations. The result of an optimization of these parameters is presented in Section 4.1.

3.8.4 Serial Interface

Any additional data processed by the OTEMS beyond that done by the FPGAs were collected through the PXIe-6363 IO card. One half of the card was connected to a NI TBX-68 unshielded

connector block which allowed for easy integration of various I/O sources. The mass flow controllers communicated with the host computer through this block. The other half of the card was connected to a shielded connector block (NI SCB-68). This block was only used in the lab as a quick way to add sensors for calibration purposes. In a field deployment only the TBX-68 would be used. The two thermistors were driven by the SCB-68.

3.9 Data Processing

This section details the data processing techniques utilized by the OTEMS leading to a flux measurement. First, some characterization procedures needed to be run at regular interval in between data collection runs. These were the wavelength characterization and the laser intensity and phase characterization. Following successful characterizations, a flux measurement could be performed. The methodology behind a velocity and concentration measurement from the collected $2f$ peak data is presented. The same methodology applies to both calibration purposes and flux measurements.

3.9.1 Pre-Run System Calibration

An accurate velocity measurement relies on a proper characterization of the amplitude in wavelength of the sweep frequency. Similarly, an accurate concentration measurement relies on a proper characterization of the laser intensity and phase. Below is the procedure followed by the OTEMS to perform both of these characterizations. Based on previous WMS experiments (Schoonbaert et al., 2014), these characterizations should be performed daily to ensure accurate flux measurements.

3.9.1.1 Wavelength Characterization

The FRR was used to record changes in wavenumber of the TDL within a sweep. These relative wavenumber changes were recorded with the modulation turned off so that only the linear wavenumber sweep induced the FRR signal. From this, the variation in wavenumber vs. sample point could be determined. One advantage of using a triangle sweep waveform is that the leading and lagging wavenumber vs. sample point curves can be accurately described by linear equations of the form $y = mx + b$.

Figure 3.9a shows the time averaged FRR signal for a 50 Hz sweep with 0.1 V amplitude. Also plotted is the corresponding time varying laser intensity. The spacing between individual interference peaks in the FRR signal is the FSR, which was determined as outlined in Section 3.5.2 to be 0.01136 cm^{-1} . These peaks were located by the LabVIEW Peak Finding VI, which locally fits a polynomial to the signal and identifies either peaks or valleys. From these data, a plot of relative wavenumber vs. sample point was generated as shown in Figure 1.9b. Each point in Figure 1.9b corresponds to a detected peak in Figure 1.9a, and is equally spaced in wavenumber on the vertical axis. The 0.1 V sweep amplitude corresponded to a wavenumber amplitude a_{sweep} of 0.109 cm^{-1} peak-to-peak.

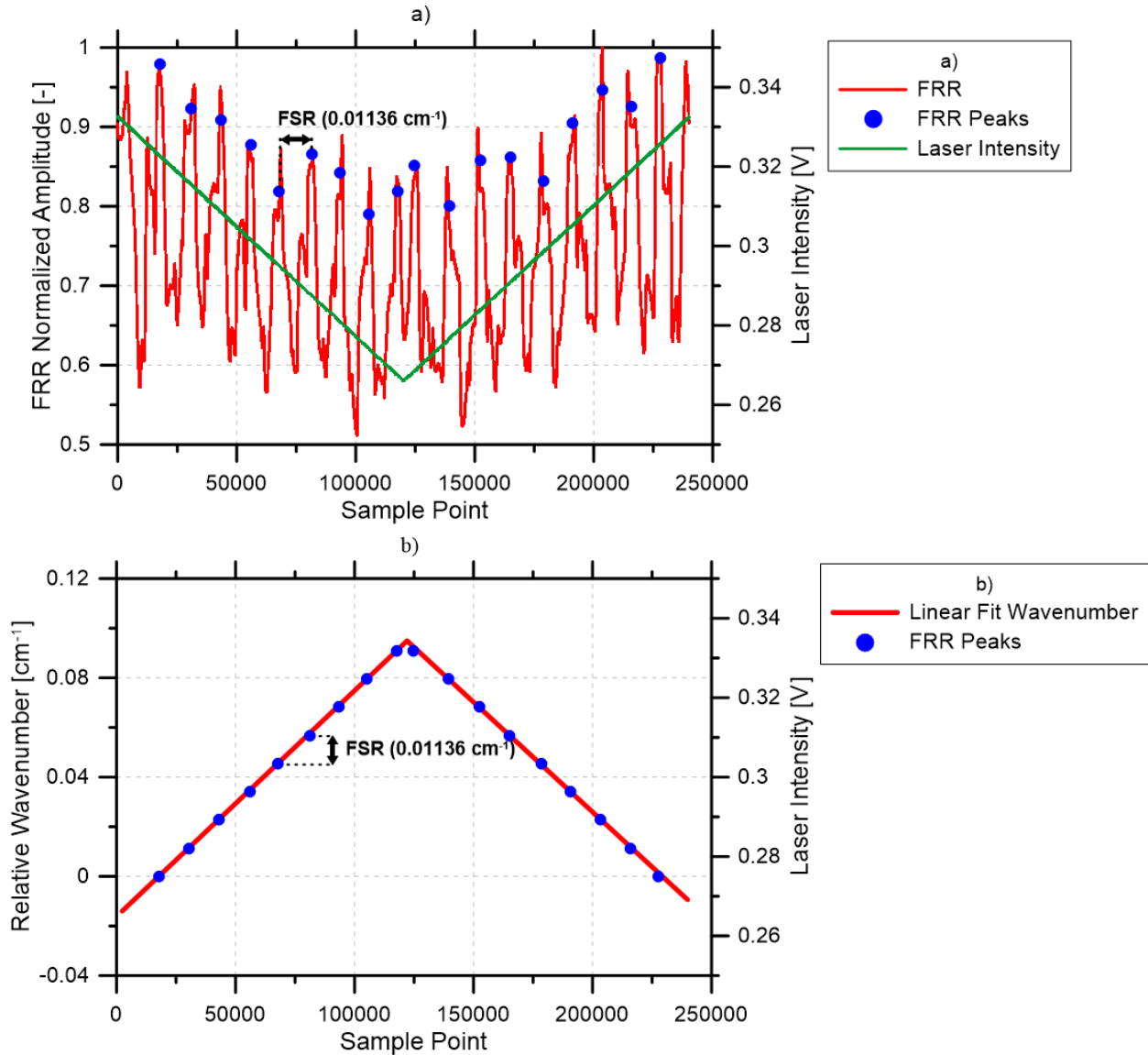


Figure 3.9: a) Time averaged signal of the FRR and laser intensity from a sweep frequency of 50 Hz with an amplitude of 0.1 V. The peaks of the FRR signal are identified by blue points. b) The FRR peaks in blue from plot a) are equally spaced on the vertical axis by the FSR to recreate the linear wavenumber sweep, with the first peak set to cm^{-1} . The red line is the combination of linear fits for both the leading and lagging sections of the sweep.

Section 3.9.2 explains how the velocity measurement relies on converting the separation between two $2f$ signals to a wavenumber shift. Consistent with equation (2.16), the $2f$ signals were discretized by the modulation period where the number of modulation periods within a sweep is based on the ratio of the modulation and sweep frequencies. The Doppler shift between the measured $2f$ signals was first calculated as a fractional multiple of modulation periods. Using

the linear fit result from Figure 3.9b, a wavenumber vs. modulation period number relation was generated. This was done by multiplying the horizontal axis in Figure 3.9b (number of sample points) by the ratio of the modulation frequency to the sample frequency used in generating the figure. To allow for the possibility of varying laser response at different sweep frequencies, separate wavelength characterizations were performed for each different sweep frequency used in this thesis.

3.9.1.2 Laser Intensity and Phase Characterization

The theoretical $2f$ features, which were computed to evaluate species concentration as per Section 3.9.3, required the amplitudes i_0 and i_2 and phases ψ_1 and ψ_2 of the absorption free intensity signal as well as the average intensity \bar{I}_0 . These values can either be measured directly in the sample pipe or inferred from secondary sources. In the present case, the amplitudes and phases of the absorption free intensity in the four sample lines were inferred from the laser reference line within the thermally stabilized enclosure.

The laser reference line and FRR were sampled by the second FPGA with only the modulation waveform driving the laser current. The values of $\bar{I}_{0_{ref}}$, $i_{0_{ref}}$, $i_{2_{ref}}$, $\psi_{1_{ref}}$, and $\psi_{2_{ref}}$ were extracted from these two lines. The intensity terms ($\bar{I}_{0_{ref}}$, $i_{0_{ref}}$, $i_{2_{ref}}$) were measured using LabVIEW's tonal analysis VIs, which also reported the average intensity as a DC term. These reference intensity values were then scaled by the average intensity of each sample pipe line to obtain \bar{I}_0 , i_0 , and i_2 for each line.

While the reference line on its own can be used to measure the intensities listed above, the phase terms require a concurrent wavelength measurement. Unfortunately, the signal from the FRR was too noisy to permit quantification of these phase terms at the high frequencies used

to modulate the laser. The interference peaks were very weak and inconsistent from trial to trial. It is believed that poor manufacturing of the fiber splices within the FRR were to blame. Both $\psi_{1_{ref}}$ and $\psi_{2_{ref}}$, and therefore ψ_1 and ψ_2 , were set to 0 for the results included in this work. However, this choice would only affect the concentration measurement and would be compensated for during calibration. The calibration results presented in Section 4.6 demonstrate that this assumption had negligible impact on the accuracy of the OTEMS in measuring concentration.

3.9.2 Velocity Measurement

A TDLAS based velocity measurement, as seen in Section 2.2, is based on quantifying Doppler shifts between an upstream and downstream sample lines within the sample pipe. The OTEMS was configured to have two upstream and two downstream sample lines. The use of a triangle waveform for the sweep led to the collection of two $2f$ features per sweep period, as the absorption feature was crossed twice within one period. The first crossing, when the laser frequency is increasing, is known as the leading; while the second, when the laser frequency is decreasing, is known as the lagging. There are therefore four leading $2f$ features and four lagging $2f$ features per sweep period, which can be compared to calculate eight Doppler shifts, of which four are independent. The nomenclature used here is based on a sample line numbering system - each line is given a number from 1 through 4. The two beams propagating upstream are sample lines 1 and 3, while the two beams propagating downstream are sample lines 2 and 4. For example, $\overline{\Delta\nu}_{12}$ [cm^{-1}] refers to the average of the leading and lagging Doppler shifts between lines 1 and 2. A positive Doppler shift indicates a flow through the sample pipe from the inlet to the outlet. In the laboratory setting, the end of the sample pipe to which the mass flow

controllers are connected is the inlet. $\Delta v_{12,lead}$ refers to the leading Doppler shift of lines 1 and 2.

Many methods were investigated to determine the Doppler shift between two individual lines. The first attempts were based on previous studies, such as (Philippe and Hanson, 1993) who fit the second harmonic profile with a fifth order polynomial. A second technique, inspired by a Voigt fit of absorption profiles in (Chang et al., 1991), attempted to fit the entire $2f$ feature with a polynomial derived from the theory presented in Section 2.1.1.2. While these methods proved successful in some cases, they required excessive user input to be properly applied to results with different sweep and modulation amplitudes. This limitation was important in the context of an operational parameter optimization, as widely different $2f$ features were investigated. A more robust method which was independent of the shape of the $2f$ feature was required.

3.9.2.1 Cross-Correlation Velocity

The OTEMS velocity measurement is done by calculating the cross-correlation between two sample lines. The cross-correlation $R_{xy}(t)$ of signals $x(t)$ and $y(t)$ is:

$$R_{xy}(t) = x(t) \star y(t) = \int_{-\infty}^{\infty} x^*(t) y(t + \tau) d\tau \quad (3.3)$$

where $x^*(t)$ is the complex conjugate of $x(t)$. The highest peak in the cross-correlation results corresponds to the lag, or shift, between the two signals. The location of this peak can thus be used to determine the Doppler shift between two sample lines. A third degree polynomial was used to fit the cross-correlation result and determine the location of its peak. This location was a non-integer multiple of modulation periods, and when multiplied by the appropriate wavelength

slope determined through Section 3.9.1.1, yielded the Doppler shift in wavenumber between the two lines. If no Doppler shift is present between two sample lines, the peak should be located in the center of the cross-correlation result. Depending on the order of the signals in the cross-correlation, a positive Doppler shift will result in the peak of the cross-correlation moving to the left or right of center. The eight Doppler shift collected from the four sample lines were averaged together, and a linear calibration (see Section 4.5) was applied to this average. The velocity was calculated according to equation (2.18).

Some pre-processing of the $2f$ signals was required before calculating the cross-correlation. An illustrative example of this process, and the impact on the cross-correlation result, is seen in Figure 3.10. If the raw $2f$ signals, shown as the solid red and blue lines in Figure 3.10a, were used in the cross-correlation, the resulting correlation function, shown in dark purple in Figure 3.10b, was overly broad and precluded accurate resolution of the Doppler shift. This effect was found to be a result of end effects in the finite signals. However, by preprocessing the raw $2f$ signals to force the starting and ending values to zero, this issue could be avoided. This was especially important at large sweep amplitudes where the wings of the $2f$ feature were captured. The ends of the $2f$ signals were therefore inspected and the greater of the two ends was subtracted from the entire signal. Any negative values were then set to 0. This produced signals such as the dotted red and blue lines in Figure 3.10a. The resultant cross-correlation of these preprocessed signals was sharply focused (as shown by the green dotted line Figure 3.10b) and was found to accurately represent the shift between the $2f$ signals for all investigated sweep amplitudes. While this procedure necessarily ignored a potentially significant portion of the collected $2f$ feature, especially at large sweep amplitudes, the results

were proven to be very robust and ensured that the collected signals could be quickly and reliably processed during the optimization study presented in Section 4.1.

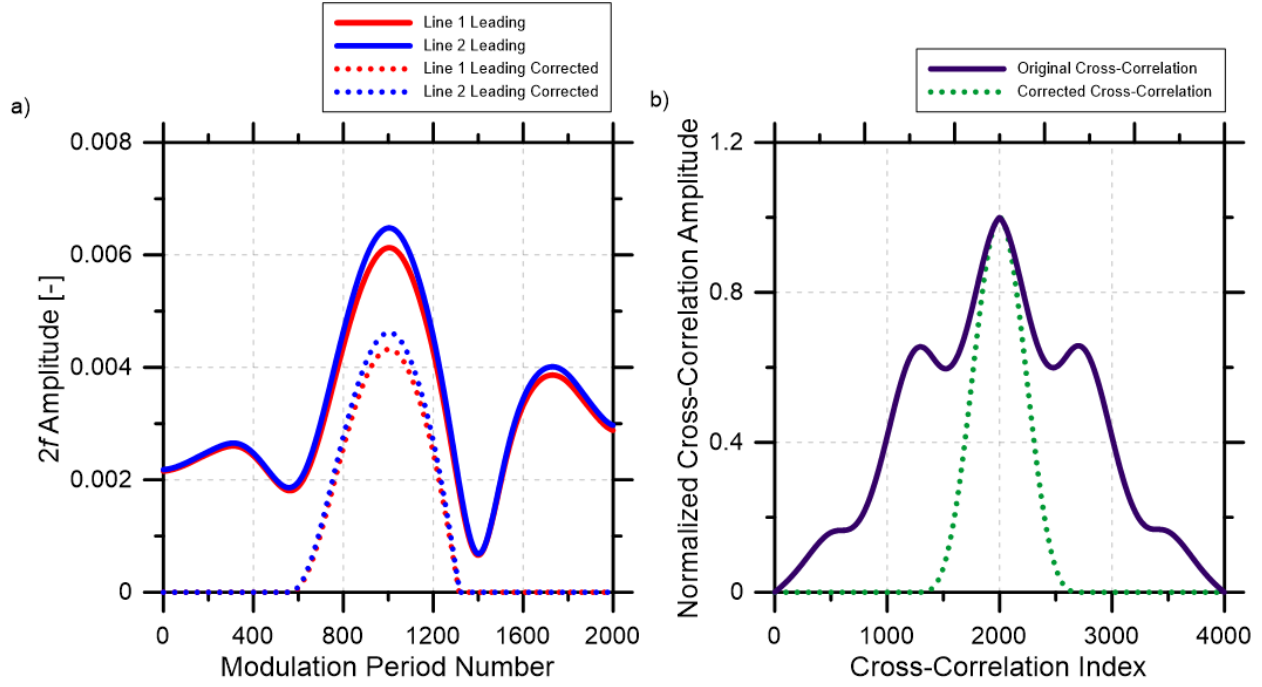


Figure 3.10: a) Collected $2f$ signal from OTEMS in solid with the corrected signals in dotted line. 0.2 V sweep @50 Hz (effective sweep amplitude of 0.23 cm^{-1}) and 0.28 V modulation @200 kHz. b) Cross-correlation results for both the original and corrected $2f$ signals.

3.9.3 Concentration

The methodology for the concentration measurement was based on Schoonbaert et al. (2014), in which a collected $2f$ peak height was compared to a four dimensional look-up table containing $2f$ peak heights for various temperatures, pressures, and oxygen concentrations based on the theory presented in Chapter 2. Based upon the average temperature of the inlet and outlet thermistors and the pressure read at the DPG, the look-up table was linearly interpolated in two dimensions to reduce it to a two dimensional table containing $2f$ peak heights and oxygen concentrations. The height of the collected $2f$ was then found within this table and a final linear interpolation was

performed to calculate the corresponding oxygen concentration. The accuracy of this method was heavily dependent on the step size chosen for each of the independent variables of temperature, pressure and concentration. Processing time to generate the table was directly related to these step sizes. The frequency at which the look-up table was updated based on laser intensity characteristics, as well as temperature and pressure, was tailored to the ability of the host computer to maintain a real-time measurement. If the concentration measurement is done in a post-processing environment, this frequency can be increased for additional accuracy. For every sweep period, 8 independent concentration measurements were made. These measurements were then averaged together to report the concentration of oxygen within the sample pipe. A linear calibration, detailed in Section 4.6, was applied to this average value.

Chapter 4 Results and Discussion

4.1 Optimal Laser Operational Parameters

As previously described, the OTEMS uses WMS, which combines a low frequency sweep and high frequency modulation with different amplitudes. To determine the best possible combination of these frequencies and amplitudes an optimization study was conducted. Two objectives were considered: the first was minimizing the standard deviation of a 1-s averaged velocity measurement (short SD), and the second was minimizing the standard deviation of a 30-s averaged velocity measurement (long SD). The former objective targeted the instantaneous precision of the measurement, while the latter prioritized the measurement drift during 10-minute intervals relevant to the intended sampling protocol during field measurements of liquid storage tanks. The velocity measurement was given priority over concentration measurement due to the anticipated difficulties in achieving the target velocity sensitivity. Preliminary results suggested that our concentration target could be reached with minimal effort.

The optimization study began by decoupling the sweep and modulation parameters and analyzing them separately. This allowed for a relatively rapid determination of both an optimal sweep frequency and amplitude as well as an optimal modulation frequency and amplitude. Two rounds of optimization were conducted, starting from a sweep frequency of 100 Hz and amplitude of 0.28 V as set by the frequency generators. This set of parameters was selected as a starting point based on initial trial experiments with the OTEMS. A parametric study of modulation frequencies and amplitudes was first conducted to find the combination with the minimum short- and long-SD. From the chosen minimum, a subsequent parametric study of

sweep frequencies and amplitudes was conducted. This process was repeated a second time, starting from the new optimized sweep parameters until the final sweep parameters were unchanged. Appendix A shows plotted results of the first round of this parametric optimization. The second round results are included below.

The optimization study was conducted in quiescent air, at ambient oxygen concentration. For every combination of frequency and amplitude that was investigated, five minutes of 1-s averaged velocity measurements were collected with the pipe ends closed-off and the cell filled with ambient air. The collected data were divided into ten 30 s duration segments. The standard deviations of the 1 s measurements during each of these 30 s segments were calculated, and the average of these 10 standard deviations was used as the first minimization objective (short SD). For the second criteria, the average measured velocity during each 30 s interval was calculated, and the optimization study sought to minimize the standard deviation of these ten, 30-s averaged values (long SD). No digital filtering was applied during these measurements.

The second round of optimization started from the optimized parameters from round 1 of $f_m=320$ kHz, $a_m=0.5$ V, $f_{sweep}=50$ Hz, and $a_{sweep}=0.1$ V, as further detailed in Appendix A. Figure 4.1 plots the results of search for optimum modulation parameters. Figure 4.1a shows that a new minimum short SD of 0.0326 m/s was found at $f_m=200$ kHz and $a_m=0.28$ V. The optimization surface for long SD shown in Figure 4.1b was noisier than the short SD surface of Figure 4.1a. A minimum long SD value of 0.011 m/s was found at $f_m=500$ kHz and $a_m=0.35$ V. However, Figure 4.1b suggests that the long SD value of 0.019 m/s at the short SD optimum settings of $f_m=200$ kHz and $a_m=0.28$ V is similar within the noise level of the surface. Thus, optimum short SD modulation parameter settings were used for a final parametric study of

optimum sweep parameters. As shown in Figure 4.2, this final optimization step confirmed the previous choices of $f_{sweep}=50$ Hz, and $a_{sweep}=0.1$ V from the short SD result.

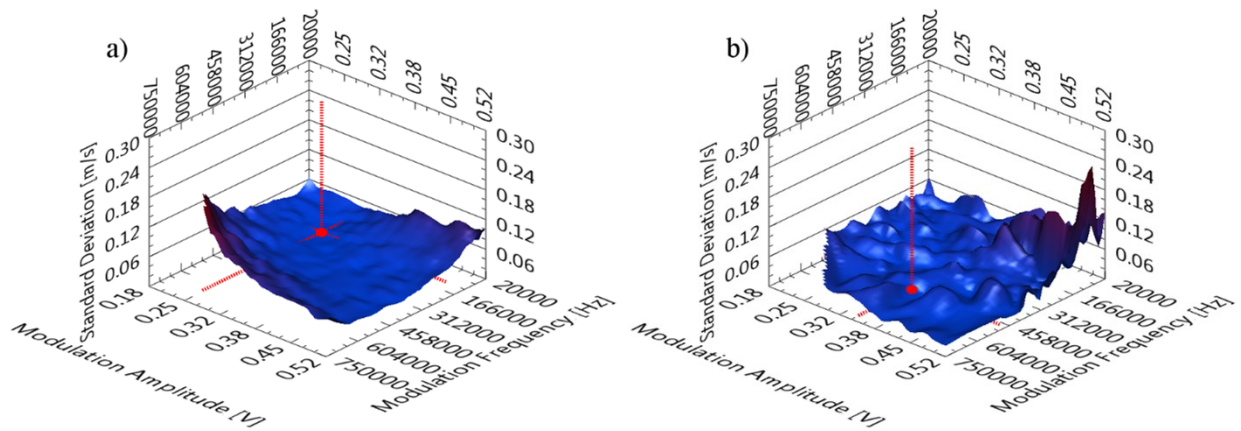


Figure 4.1: Surface plots of the parametric optimization of the OTEMS velocity measurement for varying modulation parameters at a fixed sweep of 50 Hz and 0.1 V amplitude. The minimum standard deviation is highlighted by the red point in each sub plot. a) Short SD, minimum of 0.0326 m/s at 200 kHz and 0.28 V. b) Long SD, minimum of 0.011 m/s at 500 kHz and 0.35 V.

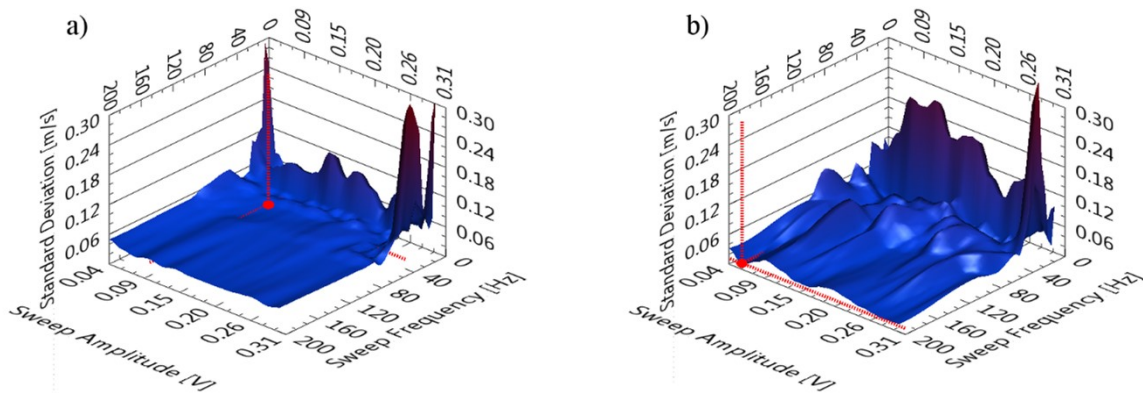


Figure 4.2: Surface plots of the parametric optimization of the OTEMS velocity measurement for varying sweep parameters at a fixed modulation of 200 kHz and 0.28 V amplitude. The minimum standard deviation is highlighted by the red point in each sub plot. a) Short SD, minimum of 0.0335 m/s at 50 Hz and 0.1 V. b) Long SD, minimum of 0.012 m/s at 200 Hz and 0.06 V.

The remainder of the results presented here were collected at the determined optimum modulation settings of $f_m=200$ kHz and $a_m=0.28$ V and sweep settings of $f_{sweep}=50$ Hz, and $a_{sweep}=0.1$ V. The surface plots included above indicate that the precision of OTEMS is not very sensitive to the selection of these operational parameters. However, it is strongly recommended that this optimization be re-examined using the long SD result once the future work suggested in Chapter 5 is addressed.

4.2 Digital Filter Selection

In an effort to improve system performance, a digital filter was implemented on the calculated $2f$ signal. The intent of this filter was to reject noise components which occurred at greater than twice the sweep frequency since the $2f$ signal was extracted twice per sweep. The filter was built using LabVIEW's zero-phase filter, configured as a lowpass Butterworth filter. The final cut-off frequency (f) was experimentally selected to minimize noise, without adversely affecting the $2f$ signal amplitude and the resultant velocity measurement. With the end caps purged with nitrogen (See Section 4.3), 10 s of unfiltered $2f$ signal with no averaging was collected. These data were then processed with various filter frequencies. As shown in Figure 4.3, the filter had a similar effect on both signal amplitude and measured velocity. In both cases, as the filter cut-off frequency was lowered, the respective $2f$ peak height and velocity results converged on fixed values until approximately 800 Hz. Below this limit, the results quickly diverged as the filter began to affect the desired $2f$ feature. From these results a cut-off frequency of 800 Hz was selected. The fast Fourier transform of the $2f$ signal, before and after filtering, is shown in Figure 4.4. Unless otherwise mentioned, this filter was enabled for all of the data and results presented here. Figure 4.5 shows sample raw and filtered $2f$ signals, which illustrates the effectiveness of the filter in removing noise.

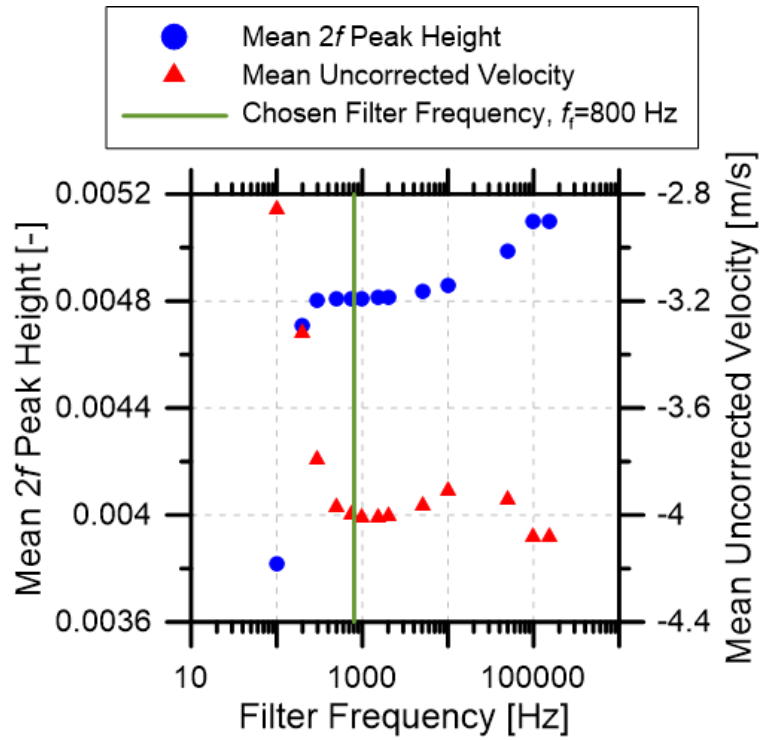


Figure 4.3: Effect of the cut-off frequency on mean $2f$ peak height and velocity when using a zero-phase change Butterworth low pass filter. Chosen filter frequency, 800 Hz, shown by green vertical line.

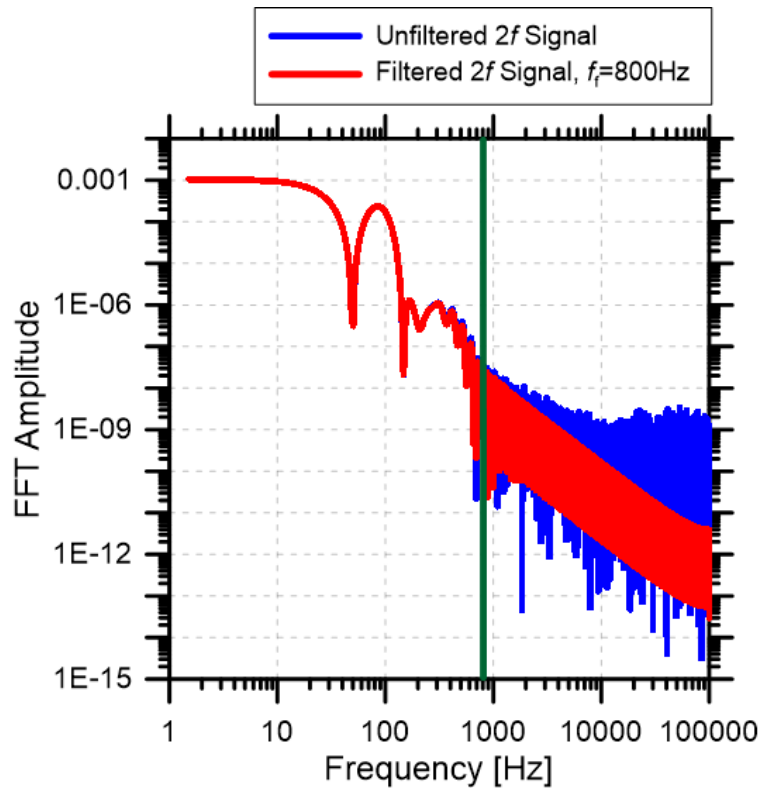


Figure 4.4: Fast Fourier Transform of a $2f$ signal with no averaging. Blue line is the unfiltered signal, red line is filtered with a lowpass cutoff of 800Hz. Cutoff frequency shown as vertical green line.

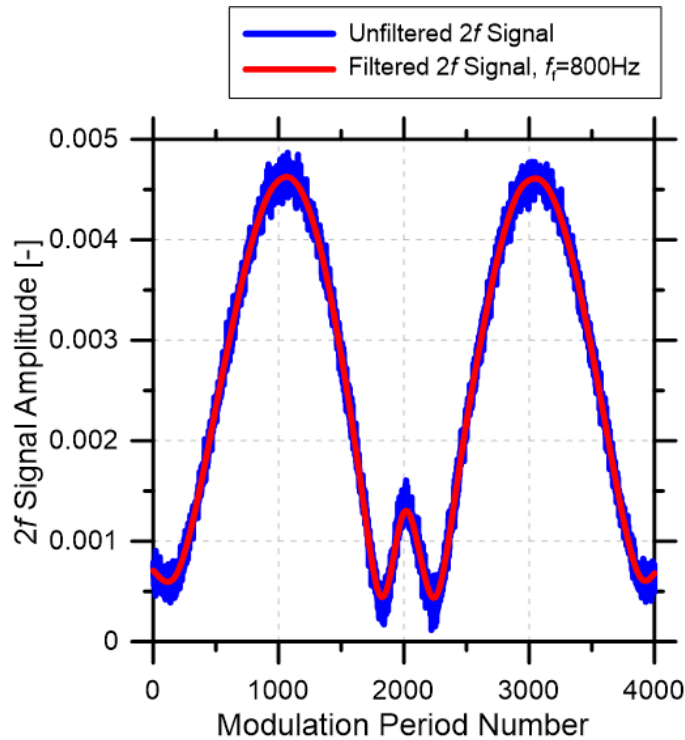


Figure 4.5: Unfiltered and filtered (filtering frequency 800Hz) $2f$ signal

4.3 End Cap Nitrogen Purging

While care was taken to minimize the distance traversed by the laser beams within the ends of the cell outside the sampling region within the pipe, it was not possible to bring this length to zero. As such, any oxygen within the end caps of the OTEMS would absorb some of the light intensity and consequently affect the $2f$ signal. While literature suggests that it may be possible to account for this length with a simple linear correction factor (Lyle, Jeffries, Hanson, et al., 2007), the capacity to purge the end capsules with a non-absorbing gas was built into the OTEMS device. This is detailed in Sections 3.6.4 and 4.3.

Figure 4.6 shows sample $2f$ signals measured with and without the end caps purged with nitrogen. Also plotted (grey line) is the measured background signal when the entire system (pipe and end caps) was purged with nitrogen. This background signal is relevant in the

discussion of OTEMS performance in Sections 4.4 & 4.7. A reduction in $2f$ peak height was evident when O_2 was purged from the end caps.

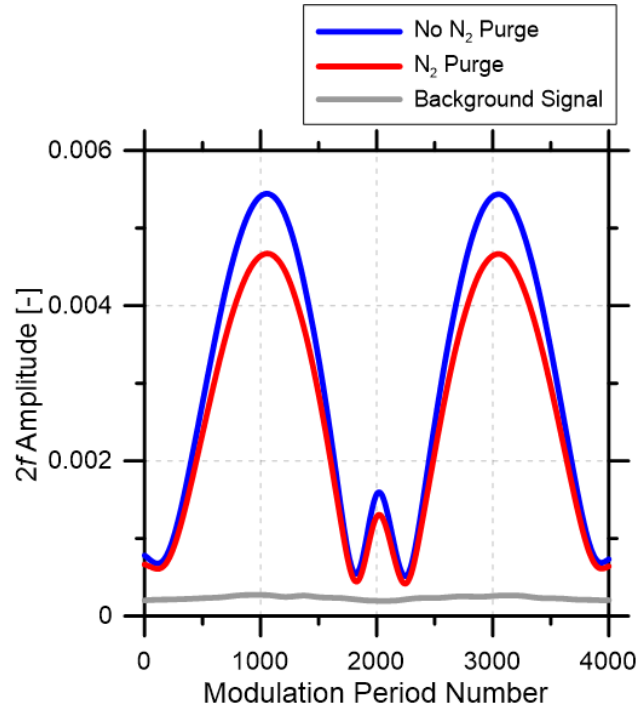


Figure 4.6: Effect of nitrogen purge in the end caps of the interrogation section on collected $2f$ signals. The gray signal is the background signal for the same sample line when the interrogation section is filled with nitrogen.

4.4 Velocity Measurement Bias and Drift

Figure 4.7 plots the measured velocity with 30-s averaging from the OTEMS over 20 hours during which the ends of the sample pipe were closed off so that the true velocity would be zero. Ideally the measured velocity should have remained at zero during this period. Instead, a time-varying bias offset of -3.19 to -4.29 m/s was observed. This result can be improved with a simple initial bias correction during calibration, producing the adjusted result shown in green. A similar zero-velocity offset was observed by Miller et al., (1996).

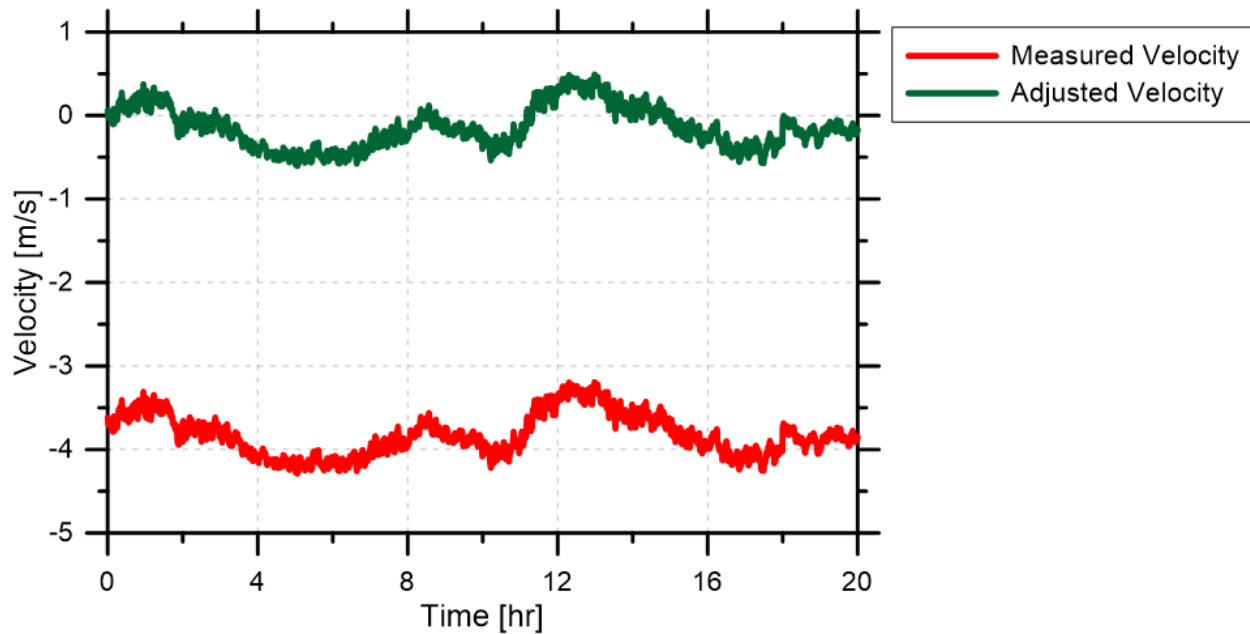


Figure 4.7: Measured velocity (red trace) with 30 s averaging over a period of 20 hours, recorded in quiescent conditions subject to room temperature changes. The green trace has been adjusted by removing the initial velocity bias present in the raw measurement.

The standard deviation of the adjusted velocity measurement over these 20 hours was 0.24 m/s. This compares favorably with the precision achieved by Lyle, Jeffries, and Hanson (2007), who reported a standard deviation of 0.22 m/s with 1-s averaging over a period of 90 s. This is the lowest standard deviation of all the studies summarized in Table 2.1. If we make an equal comparison to Lyle, Jeffries, and Hanson (2007) using the same averaging and measurement period (1-s averages, 90 s measurement), the OTEMS improved this result by a factor of 5, achieving a standard deviation of 0.044 m/s. This result is especially significant when considering that in the system of Lyle et al. the intensity of the laser light was measured by directly irradiating detectors, as opposed to the fiber recoupling scheme adopted by OTEMS. The greater precision of the former scheme has long been recognized (Miller et al., 1996), as it leads to significantly higher SNR and is less susceptible to mechanical disturbances. Due to the hazardous location around storage tanks, the recoupling scheme presents a significant safety advantage.

The data presented in Figure 4.7 reveal that the precision of the adjusted velocity result is dominated by drift. In the short-term, this drift can be relatively easily removed by repetitively taking a new zero velocity bias measurement. In the field, this could be accomplished by periodically closing valves at the end of the sample pipe and recording any non-zero velocity bias. The measured velocity during this time would be recorded as the new “zero bias”. Velocity measurements could then be corrected for drift by linearly interpolating and applying a bias correction during the interval between subsequent re-zeroing events. The blue curve in Figure 4.8 shows the achieved result when this re-zeroing procedure is applied at 10 minute intervals. The standard deviation of the velocity measurement when implementing this re-zeroing process was 0.07 m/s over 20 hours. The interval between re-zeroing could be adjusted based on the dynamics of the tank to which the system is connected.

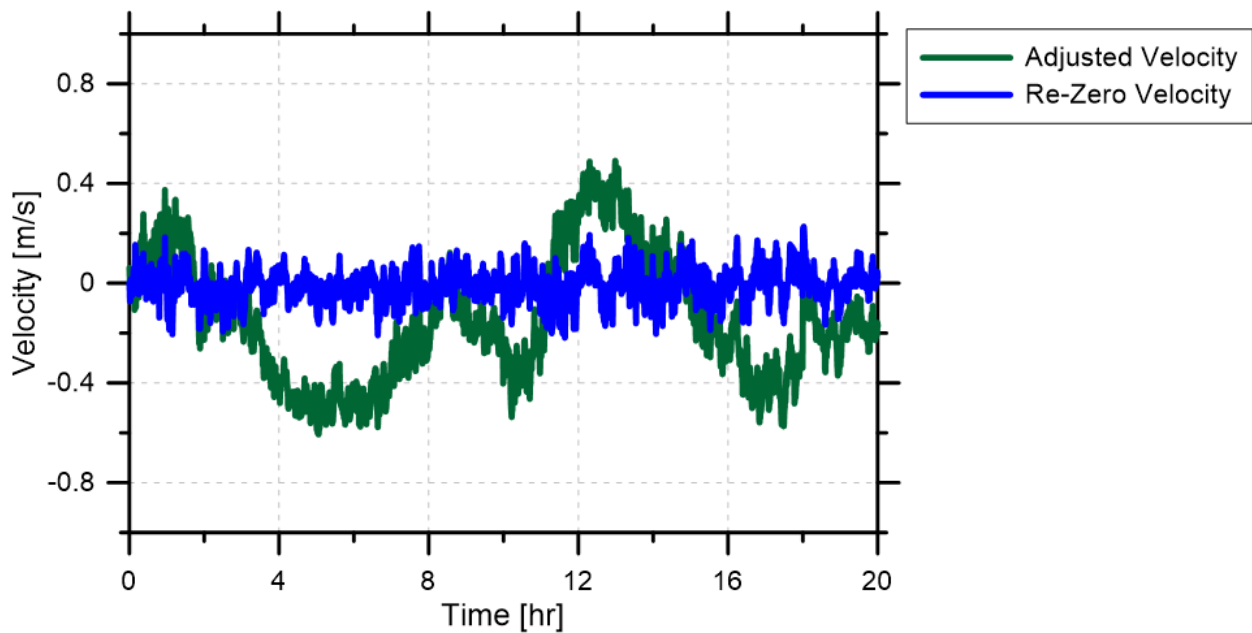


Figure 4.8: Adjusted velocity measurement with 30 s averaging over a period of 20 hours, recorded in quiescent conditions subject to room temperature changes. The re-zeroed velocity measurement in blue is the same data but with 10 minute long intervals between zeros.

4.5 Velocity Calibration

The digital mass flow controllers (MFC) mentioned earlier were used to flow a range of velocities through the OTEMS system at atmospheric oxygen concentrations. The target flow velocities were randomized throughout the test. At each tested velocity, the system was allowed to settle for 90 s and then ten minutes of $2f$ data were taken with 30 s averaging of the signals producing 20 independent measurements. In addition, to account for system drift during the calibration, the re-zeroing process described in Section 4.4 was performed automatically at ten minute intervals by the host computer between the set points of the velocity calibration.

Velocities were calculated using both leading and lagging $2f$ peaks for all four pairs of sample lines. These eight velocity readings were then averaged to find the single mean velocity. This mean velocity was calculated for each of the 20 data points, and the standard deviation of these data over the 10 minute sample was calculated. This calibration was repeated nine times over multiple days. The results from all of the nine runs are presented in Figure 4.9.

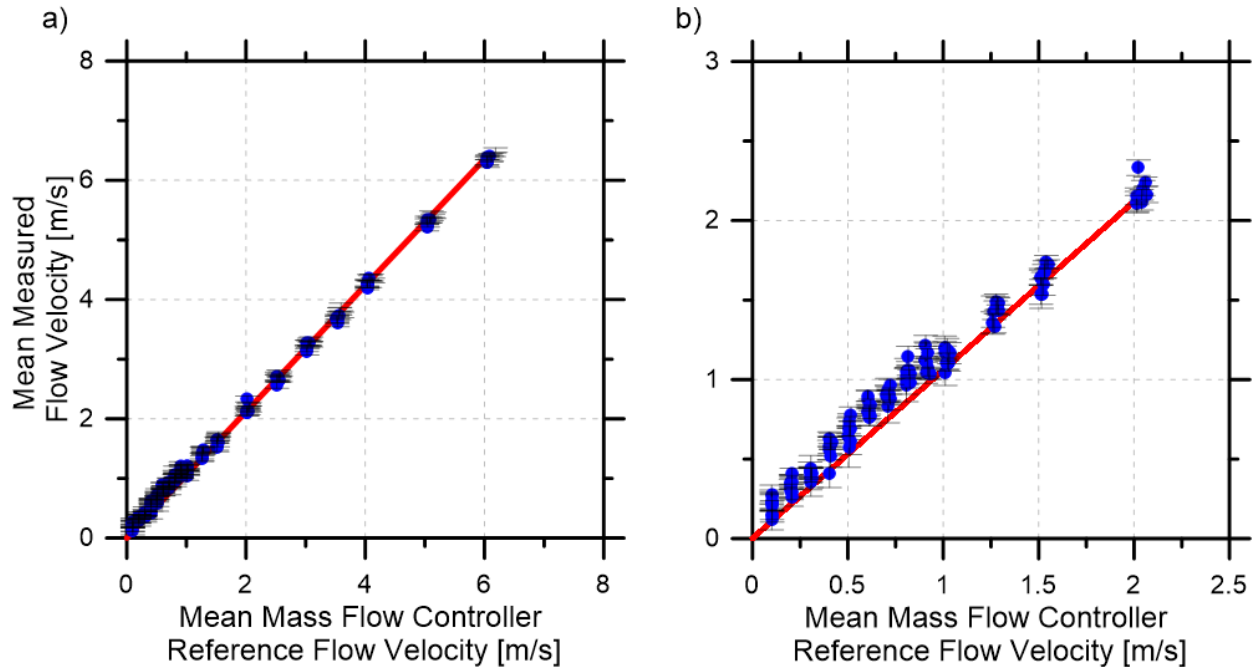


Figure 4.9: Mean measured velocity (zero corrected) by the OTEMS with respect to the reference velocity determined by the digital mass flow controllers. Plot a) displays the results from 0 to 6 m/s bulk velocity with a linear line of best fit. Plot b) displays the results from 0 to 2 m/s bulk velocity with the same linear line of best fit as in a). Error bars on both plots are the standard deviation of the 20 data points within each sample.

As shown in Figure 4.9a, the velocity calibration is very linear. However, a close-up view of the low velocity region from 0 to 2 m/s (Figure 4.9b) reveals some minor deviation from the linear fit. This variation is attributed to the changing shape of the velocity profile within the pipe at low velocity. While the symmetric cross-arrangement of the beams is such that each beam crosses a significant section of the flow profile, the beams are concentrated in the middle of the pipe. Assuming a transition from laminar to turbulent flow occurs around a Reynold's number of 3000, this transition should occur around 1 m/s bulk velocity at room temperature. Such a transition is observable in the velocity calibration results. Given the possible fluctuations of fluid viscosity with temperature and gas composition, corrections for this effect would require an extensive methodology that was not considered for the current OTEMS system. However, the

deviation in velocity from the calibration curve is small, and is negligible relative to the system drift. The calibration also removes any end effects, such as recirculation, caused by the imposed flow geometry.

4.6 Concentration Calibration

Similarly to the velocity calibration, the OTEMS' concentration measurement was calibrated in a controlled setting using digital mass flow controllers. These MFCs were used to mix various ratios of air and pure nitrogen so as to vary the concentration of oxygen within the sample pipe. Oxygen mole fractions from 2.5 % to 21 % were tested at eight discrete steps. The intended use of the OTEMS precludes the necessity for calibration above atmospheric concentration of oxygen. Each concentration of oxygen was tested at 4 flow rates: 0.5 m/s, 1 m/s, 1.5 m/s, and 2 m/s. At each set point the flow was maintained for 250 s to allow the MFCs to settle and flush the sample pipe of the previous mixture. The measured $2f$ signals were averaged for 5 seconds. Figure 4.10 shows the results of this concentration calibration along with a linear best fit line. The results demonstrated that the OTEMS concentration measurement is highly repeatable at the tested flow rates. The calculated error bars are very small (0.002 % to 0.11 % absolute standard deviation) and this level of accuracy was deemed more than sufficient for the intended application to measure emissions from liquid storage tanks.

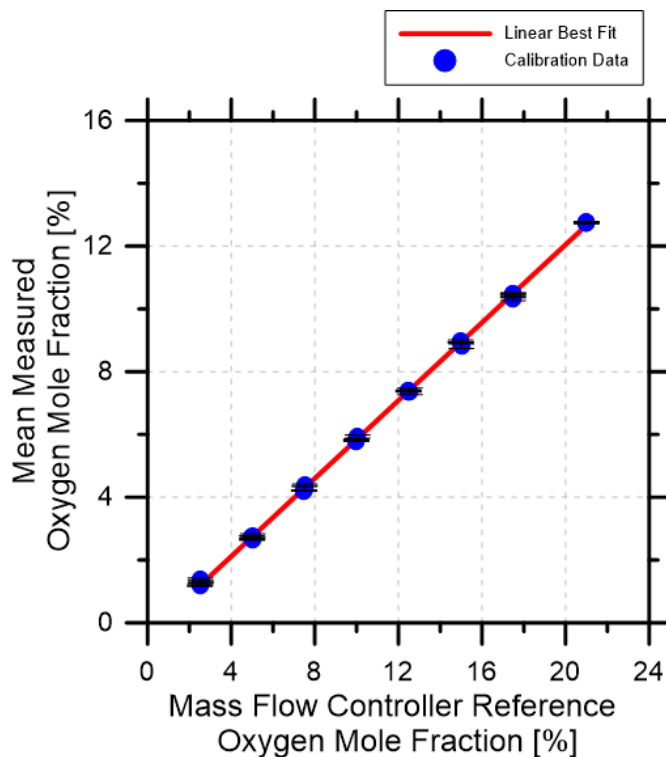


Figure 4.10: Mean measured oxygen mole fraction with respect to reference oxygen mole fraction as determined by the mass flow controllers. Each mole fraction set point was done at 4 flow velocities: 0.5, 1.0, 1.5, and 2.0 m/s.

4.7 Mass Flux Results

The current performance of the OTEMS was tested at low flow velocities to simulate its expected performance on a small storage tank which is the target of upcoming field tests. These tests were performed similarly to the concentration calibration procedure. Flow velocities of 0.5 m/s, 1.0 m/s, 1.5 m/s, and 2 m/s were used in combination with oxygen mole fractions ranging from 2.5% to 21%. These combinations represent situations of both high and low mass flux of VOCs, which would be similar to working and standing losses respectively for an active tank. It is important for the OTEMS to perform well in each scenario, and an understanding of this performance is crucial to a precise and accurate quantification of total VOC flux.

Figure 4.11 plots the measured concentrations made by the OTEMS (orange circles) overlaid on concentration (green dotted line) specified by the mass flow controllers. The correspondence of measured and specified O_2 concentrations is very good over the full range of operation. Unfortunately, the same cannot be said of the velocity measurements. Figure 4.12 shows that as the fraction of oxygen is reduced below 21%, the velocity measurement is adversely affected. At O_2 volume fractions as low as 2.5%, the velocity measurement is well off target, reaching below -20 m/s. This is a fundamental problem for the current system that precludes its use in the target application without further improvements.

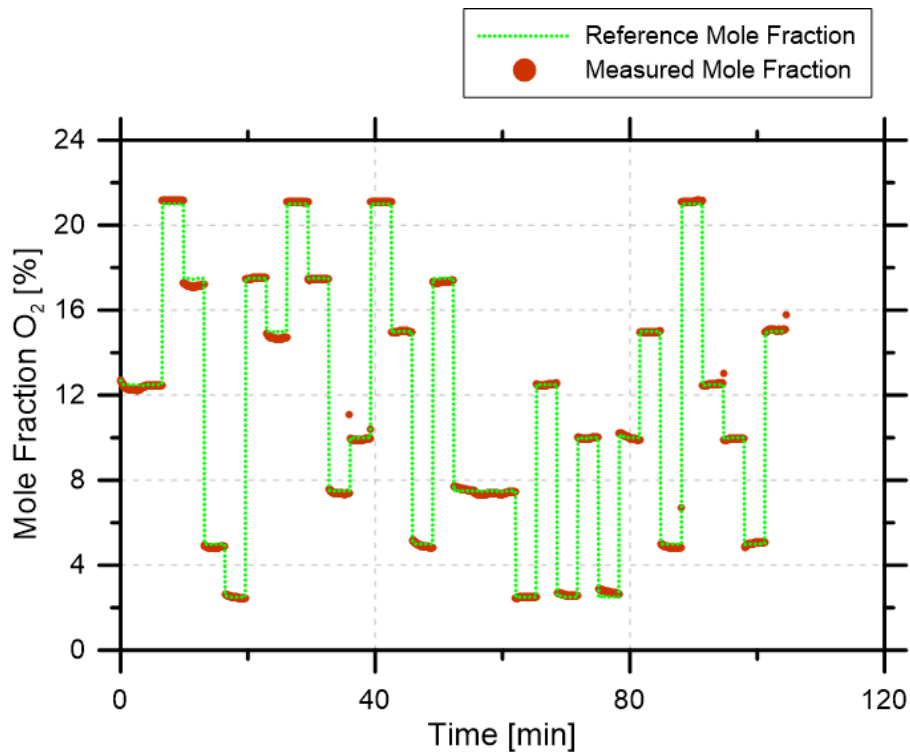


Figure 4.11: Comparison of measured and specified oxygen mole fractions in the OTEMS during a flux experiment. Dotted green line is the reference mole fraction of oxygen as reported by the MFCs.

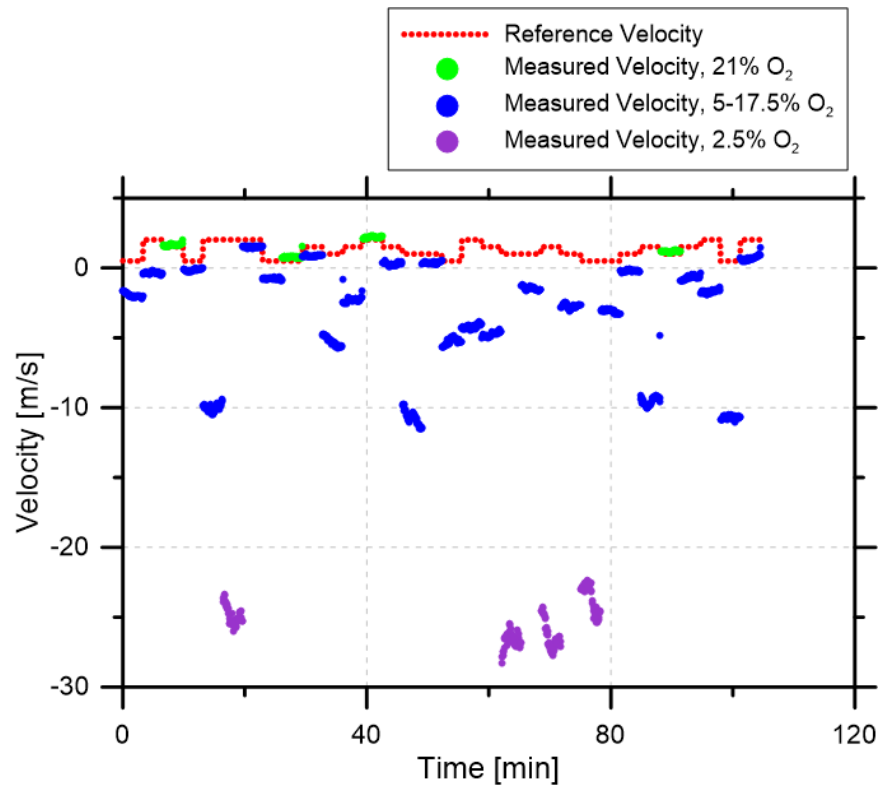


Figure 4.12: Velocity measurement of the OTEMS during a varied mass flux experiment. Velocities are grouped by colour based on the volume fraction of oxygen during the measurement. The dotted red line is the reference bulk velocity as reported by the MFCs.

Careful inspection of Figure 4.12 reveals that only the four velocity measurements made at 21 % oxygen are accurate to the requested value. The relationship between measured velocity and oxygen fraction is better shown in Figure 4.13, which shows how the error of the velocity measurement increases with decreasing oxygen fraction.

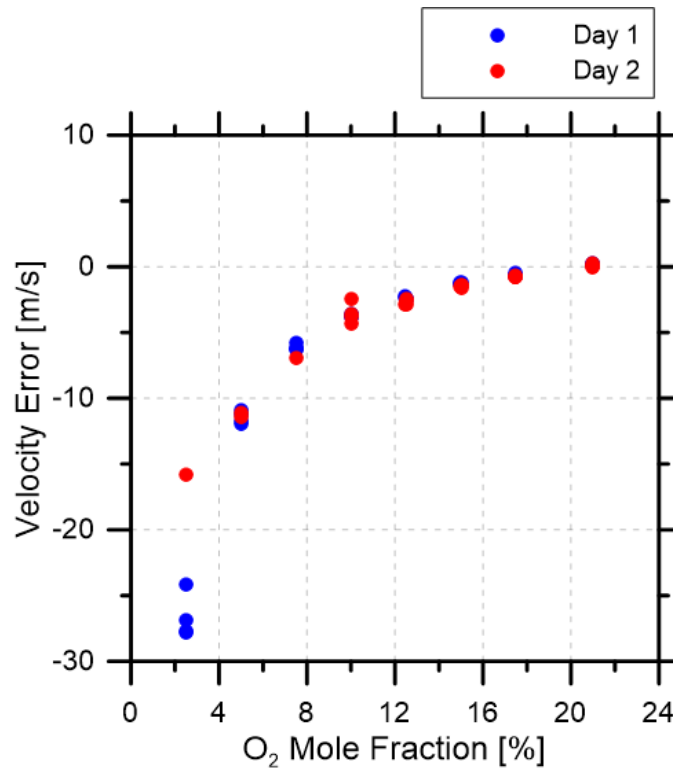


Figure 4.13: Error of the mean velocity measurement (from the MFC reference velocity) with changing oxygen mole fraction. The oxygen mole fraction is the MFC reported value. For each mole fraction value, four different velocity values were specified: 0.5, 1.0, 1.5, and 2.0 m/s. Data from two subsequent days is presented.

The presence of a distinct relationship between oxygen fraction and error in the velocity measurement may suggest that background signals begin to skew the $2f$ shape as the absorption drops and the $2f$ signal is reduced. As shown in Figure 4.14, inspection of the $2f$ signals at the highest and lowest oxygen mole fractions reveals a noticeably lower SNR at 2.5% oxygen fraction.

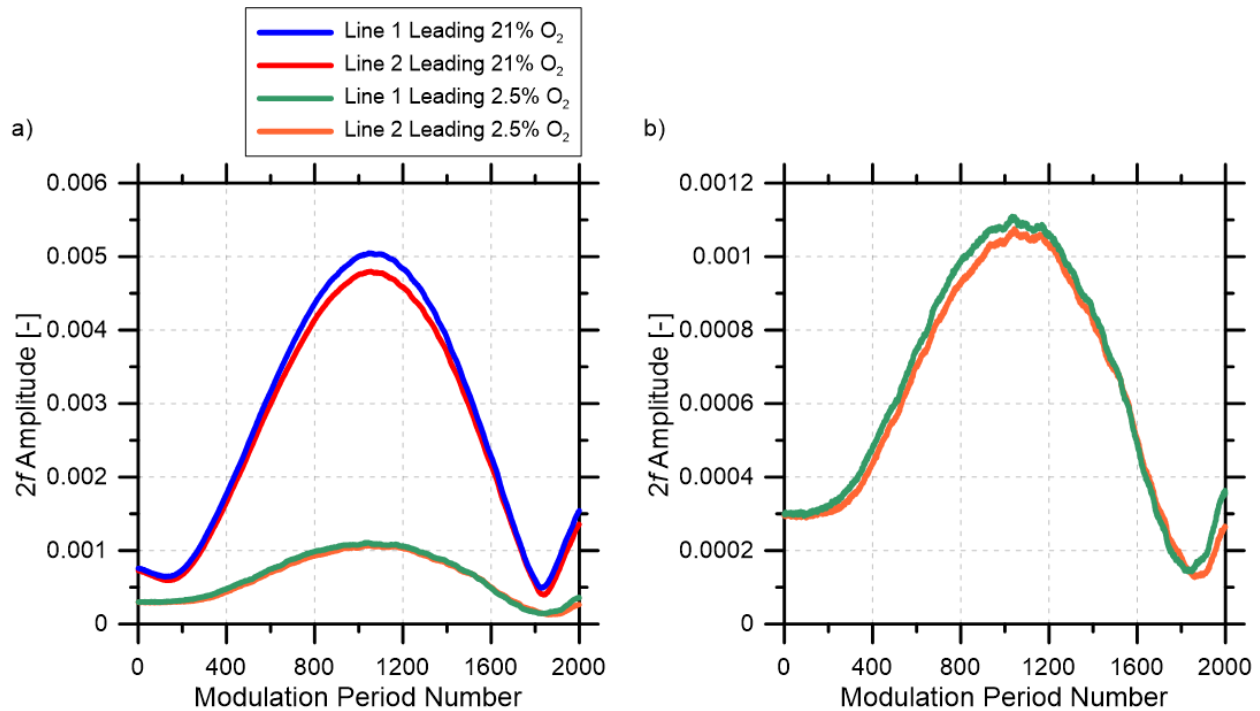


Figure 4.14: Comparison of the $2f$ signal in two lines for high and low oxygen mole fractions (21% and 2.5% respectively). Subplot b) shows the decreased SNR in the $2f$ signal at 2.5% oxygen relative to 21%.

While in principle it might be possible to calibrate for the observed effect, preliminary experiments suggest that the required calibration curves vary with the system drift such that corrections may not be simple to implement. The two sets of data presented in Figure 4.13 demonstrate how the relationship between oxygen mole fraction and velocity error changed between two subsequent days. Based on the observed signals in Figure 4.14, it is believed that the OTEMS velocity measurement at low oxygen concentrations is currently limited by SNR. This limitation must be overcome before the current system could be applied in the target application, as the highest emissions occur at low oxygen concentrations. Efforts to address this problem by boosting signal to noise levels is the subject of ongoing work, as briefly discussed in Section 5.1.

Nevertheless, the OTEMS as described above shows promise as an intrinsically safe device capable of accurately measuring a continuous mass flux of gas mixtures containing

oxygen. A 30 s standard deviation of 0.07 m/s (with rezeroing) and 0.24 m/s (without rezeroing) at 21% oxygen mole fraction is a significant improvement upon previous attempts at TDLAS velocimetry under any operating conditions reported thus far. The critical limitations of the current system under changing oxygen concentrations are a unique result that has not been observed previously. This is currently being investigated in follow-up work to this thesis. To the best of our knowledge, this work is the first to significantly alter the concentration of the detected absorption species.

Chapter 5 Conclusions

An intrinsically safe fiber-coupled low velocity mass flux sensor based on tunable diode laser absorption spectroscopy was developed for quantifying the mass flux from hydrocarbon storage tank vents. The sensor targeted an oxygen absorption peak near 764 nm. Wavelength modulation spectroscopy with second harmonic detection was used. Velocity and concentration of oxygen were measured continuously. Mass flux of VOCs from storage tanks could be calculated by combining the measured velocity with the difference in oxygen concentration from ambient levels.

A four beam arrangement was used within a 1.6 m long sample pipe. Each beam was used to measure the concentration of oxygen in the pipe, while combinations of upstream and downstream propagating beams were used to measure velocity. The free-space beams were re-coupled into multi-mode fiber to meet safety requirements that would preclude the use of electronics in the immediate vicinity of a hydrocarbon liquid storage tank. When required, long fibers and co-axial cables were used to validate the sensor's capacity to be deployed to a realistic field site. The sample pipe was stiffened to minimize beam deflections. Pure nitrogen purged the end caps of oxygen to avoid absorption outside of the sample pipe.

The fiber optic network and the reference cell used by the system were thermally stabilized within the base station. The reference cell was used to lock on to the absorption feature. This process was independent of the oxygen concentration in the sample pipe. A field programmable gate array was used in conjunction with an analog to digital converter to sample

signals at 120 MHz. The FPGA was configured to calculate the $2f$ signal for all four incoming signals simultaneously. The host computer applied a zero phase Butterworth low-pass filter with a cut-off frequency of 800 Hz to the $2f$ signals to reduce noise.

A standard deviation for the velocity measurement of 0.24 m/s was achieved over a period of 20 hours with 30-s averages after optimizing the operational parameters of the wavelength modulation spectroscopy technique. A rezeroing process was developed to further improve velocity precision, and a standard deviation of 0.07 m/s was achieved within 10 minute intervals. The previous best velocity precision in the literature was reported as 0.24 m/s when calculated from 1-s measurements over a 90-s period (Lyle, Jeffries, and Hanson, 2007). The present OTEMS achieved a precision of 0.044 m/s when calculated on an identical basis. This improvement is particularly remarkable given the use of light recoupling into optical fiber in OTEMS, which is intrinsically more challenging than directly measuring the intensity of the free space beam. This latter approach would significantly improve SNR at the cost of intrinsic safety. The OTEMS was also shown to be capable of accurately measuring oxygen fractions, where a linear calibration revealed an absolute standard deviation of less than 0.11% for volume fractions between 2.5 and 21%. However, a change in oxygen fraction was found to introduce a significant bias to the velocity measurement. This is an important limitation of the current system that precludes its use (in current form) for the intended target application of measuring VOC emissions from liquid hydrocarbon storage tanks.

5.1 Future Considerations

Prior to deploying the OTEMS for field measurements, a thorough understanding of the aforementioned relationship between the measured velocity and oxygen volume fraction is

required. While it has been shown that a temporary calibration may yield adequate results, this is not a reliable solution as the lifetime of the calibration is as of yet unknown. To counteract the influence of the background on the velocity measurement at low oxygen concentrations, changes are being undertaken to increase the SNR of the sample lines. The principal avenue to increase SNR is through careful amplification of the detected intensities, without amplifying the background. It is expected that any solution to the aforementioned problem will reduce the static offset present in the velocity measurement. The influence of multi-mode capture fibers on the background also warrants investigation. Removing these fibers at the capture optics and replacing them with detectors would likely reduce measurement drift, but would introduce additional complexities to ensure that the OTEMS remains safe to operate in a hazardous location. Beyond this, a full outdoor stress test should be conducted. With adequately protected launch fibers the OTEMS is otherwise ready for a field deployment. This would allow for crucial data to be collected on the transient behaviour of liquid hydrocarbon storage tanks and ultimately lead to updated emission models, as well as vital guidance for environmental policy decisions.

References

- Abella, I.D. and Cummins, H.Z., (1961). Thermal Tuning of Ruby Optical Maser. *J. Appl. Phys.* 32:1177.
- AER, (2014). Report of Recommendations on Odours and Emissions in the Peace River Area. 2014 ABAER 005, Calgary, AB, Alberta Department of Energy. Available at: <https://www.aer.ca/documents/decisions/2014/2014-ABAER-005.pdf>
- AER, (2015). ST102: Facility List. <http://www.aer.ca/data-and-publications/statistical-reports/st102> (accessed May 25, 2015)
- Allen, M., Davis, S., Kessler, W., Mcmanus, K., Sonnenfroht, D., and Introduction, I., (1994). Velocity Field Imaging in Supersonic Reacting Flows near Atmospheric Pressure. . 32:1676–1682.
- American Petroleum Institute, (1952). *Symposium on Evaporation Loss of Petroleum From Storage Tanks*. In Papers Presented During the 32nd Annual Meeting of the API. Chicago, IL.
- API, (1993). Documentation File for API Manual of Petroleum Measurement Standards Chapter 19.1 - Evaporative Loss From Fixed Roof Tanks [API Bulletin 2518].
- Arroyo, M.P., Langlois, S., and Hanson, R.K., (1994). Diode-laser absorption technique for simultaneous measurements of multiple gasdynamic parameters in high-speed flows containing water vapor. *Appl. Opt.* 33:3296–307.
- Bomse, D., Stanton, A., and Silver, J., (1992). Frequency modulation and wavelength modulation spectroscopies: Comparison of experimental methods using a lead-salt diode laser. *Appl. Opt.* 31:718 – 731.
- Byer, R.L., Gustafson, E.K., and McDaniel, J.C., (1981). CARS Measurement of Velocity in a Supersonic Jet. *IEEE J. Quantum Electron.* QE-17:2258–2259.
- Cassidy, D.T. and Reid, J., (1982). High-sensitivity detection of trace gases using sweep integration and tunable diode lasers. *Appl. Opt.* 21:2527–2530.
- Cattolica, R.J., Gallagher, R.J., and Anderson, J.B., (1978). Aerodynamic Separation of Gases by Velocity Slip in Freejet Expansions. *AIAA J.* 17:344–355.
- Chambers, A.K., Strosher, M., Wootton, T., Moncrieff, J., and McCready, P., (2008). Direct measurement of fugitive emissions of hydrocarbons from a refinery. *J. Air Waste Manag. Assoc.* 58:1047–56.
- Chang, A.Y., Battles, B.E., and Hanson, R.K., (1990). Simultaneous measurements of velocity,

- temperature, and pressure using rapid cw wavelength-modulation laser-induced fluorescence of OH. *Opt. Lett.* 15:706–708.
- Chang, A.Y., Dirosa, M.D., Davidson, D.F., and Hanson, R.K., (1991). Rapid tuning cw laser technique for measurements of gas velocity, temperature, pressure, density, and mass flux using NO. *Appl. Opt.* 30:3011–22.
- Chang, L., Strand, C., Jeffries, J., Hanson, R.K., Diskin, G., Gaffney, R., and Capriotti, D., (2011). Supersonic Mass Flux Measurements via Tunable Diode Laser Absorption and Non-Uniform Flow Modeling. *49th AIAA Aerosp. Sci. Meet. Incl. New Horizons Forum Aerosp. Expo.* 49:AIAA 2011–1093.
- Chang, L.S., Jeffries, J.B., and Hanson, R.K., (2010). Mass Flux Sensing via Tunable Diode Laser Absorption of Water Vapor. *AIAA J.* 48:2687–2693.
- Cheng, S., Zimmermann, M., and Miles, R.B., (1983). Supersonic-nitrogen flow-field measurements with the resonant Doppler velocimeter. *Appl. Phys. Lett.* 43:143–145.
- Clearstone Engineering Ltd., (2014a). UOG Emissions Inventory Volume 1: Overview of the GHG Emissions Inventory. Gatineau, QC, Environment Canada.
- Clearstone Engineering Ltd., (2014b). UOG Emissions Inventory Volume 3: UOG Emissions Inventory Methodology Manual. Gatineau, QC, Environment Canada.
- Dasch, C.J. and Sell, J.A., (1986). Velocimetry in laminar and turbulent flows using the photothermal deflection effect with a transient grating. *Opt. Lett.* 11:603–605.
- Davidson, D.F., Chang, A.Y., Dirosa, M.D., and Hanson, R.K., (1991). Continuous wave laser absorption techniques for gasdynamic measurements in supersonic flows. *Appl. Opt.* 30:2598–2608.
- Drain, L.E., (1980). *The laser doppler technique*. New York, J. Wiley.
- Ferry, R.L. and Kissell, J.R., (2010). Manual of Petroleum Measurement Standards Chapter 19.1 Evaporative Loss from Fixed-Roof Tanks. 4th ed., Washington, D.C., American Petroleum Institute (API).
- Gordley, L.L., Marshall, B.T., and Allen Chu, D., (1994). Linepak: Algorithms for modeling spectral transmittance and radiance. *J. Quant. Spectrosc. Radiat. Transf.* 52:563–580.
- Hecht, E., (2002). *Optics* 4th ed. A. Black, ed. San Francisco, CA, Pearson Education Limited.
- Herring, G.C., Fairbank, W.M., and She, C.Y., (1981). Observation and measurement of molecular flow using stimulated Raman gain spectroscopy. *IEEE J. Quant. Elect.* QE-17:443–446.
- Hiller, B., Booman, R.A., Hassa, C., and Hanson, R.K., (1984). Velocity visualization in gas flows using laser-induced phosphorescence of biacetyl. *Rev. Sci. Instrum.* 55:1964–1967.
- Hiller, B. and Hanson, R.K., (1988). Simultaneous planar measurements of velocity and pressure fields in gas flows using laser-induced fluorescence. *Appl. Opt.* 27:33–48.

- Hiller, B., McDaniel, J.C., Rea, E.C., and Hanson, R.K., (1983). Laser-induced fluorescence technique for velocity field measurements in subsonic gas flows. *Opt. Lett.* 8:474–476.
- Jennings, D.E., (1980). Absolute line strengths in v_4 , 12CH_4 , a dual-beam diode laser spectrometer with sweep integration.pdf. *Appl. Opt.* 19:2695–2700.
- Li, F., Yu, X., Cai, W., and Ma, L., (2012). Uncertainty in velocity measurement based on diode-laser absorption in nonuniform flows. *Appl. Opt.* 51:4788–97.
- Lyle, K., (2005). Development of a real-time diode-laser mass flux sensor for simultaneous measurement of density. (*Ph.D. Thesis*). Stanford University.
- Lyle, K.H., Jeffries, J.B., and Hanson, R.K., (2007). Diode-Laser Sensor for Air-Mass Flux 1: Design and Wind Tunnel Validation. *AIAA J.* 45:2204–2212.
- Lyle, K.H., Jeffries, J.B., Hanson, R.K., and Winter, M., (2007). Diode-Laser Sensor for Air-Mass Flux 2: Non-Uniform Flow Modeling and Aeroengine Tests. *AIAA J.* 45:2213–2223.
- Maiman, T.H., (1960). Stimulated Optical Radiation in Ruby. *Lett. to Nat.* 187.
- McDaniel, J.C., Hiller, B., and Hanson, R.K., (1983). Simultaneous multiple-point velocity measurements using laser-induced iodine fluorescence. *Opt. Lett.* 8:51–53.
- Measures, R.M., (1968). Selective Excitation Spectroscopy and Some Possible Applications. *J. Appl. Phys.* 39:5232.
- Miles, R.B., Udd, E., and Zimmermann, M., (1978). Quantitative flow visualization in sodium vapor seeded hypersonic helium. *Appl. Phys. Lett.* 32:317–319.
- Miller, M., Allen, M., and Connors, T., (1998). Design and flight qualification of a diode laser-based optical mass flux sensor. *34th AIAA/ASME/SAE/ASEE Jt. Propuls. Conf. Exhib.*
- Miller, M.F., Kessler, W.J., and Allen, M.G., (1996). Diode laser-based air mass flux sensor for subsonic aer propulsion inlets. *Appl. Opt.* 35:4905–4912.
- Moosmüller, H., Herring, G.C., and She, C.Y., (1984). Two-component velocity measurements in a supersonic nitrogen jet with spatially resolved inverse Raman spectroscopy. *Opt. Lett.* 9:536–8.
- Nie, Y., Hane, K., and Gupta, R., (1986). Measurements of very low gas flow velocities by photothermal deflection spectroscopy. *Appl. Opt.* 25:3247–3252.
- Olson, M.L., Griebble, D.L., and Griffiths, P.R., (1980). Second Derivative Tunable Diode Laser Spectrometry for Line Profile Determination I. Theory. *Appl. Spectrosc.* 34:50–56.
- Paul, P.H., Lee, M.P., and Hanson, R.K., (1989). Molecular velocity imaging of supersonic flows using pulsed planar laser-induced fluorescence of NO. *Opt. Lett.* 14:417–9.
- Philippe, L.C. and Hanson, R.K., (1991). Laser-absorption mass flux sensor for high-speed airflows. *Opt. Lett.* 16:2002–4.

- Philippe, L.C. and Hanson, R.K., (1993). Laser diode wavelength-modulation spectroscopy for simultaneous measurement of temperature, pressure, and velocity in shock-heated oxygen flows. *Appl. Opt.* 32:6090–103.
- Picard, D. and Johnson, M.R., (2011). Convective Evaporation Losses from Underground Storage Tanks. Calgary, AB, Petroleum Technology Alliance of Canada (PTAC).
- Reid, J. and Labrie, D., (1981). Second-Harmonic Detection with Tunable Diode Lasers - Comparison of Experiment and Theory. *Appl. Phys.* 210:203–210.
- Reid, J., Shewchun, J., Garside, B.K., and Ballik, E.A., (1978). High sensitivity pollution detection employing tunable diode lasers. *Appl. Opt.* 17:300–7.
- Rieker, G.B., (2009). WMS for measurements of gas temperature and concentration in harsh environments.
- Rose, A. and Gupta, R., (1985). Application of photothermal deflection technique to flow-velocity measurements in a flame. *Opt. Lett.* 10:532–534.
- Rothman, L.S., Gordon, I.E., Barbe, A., Benner, D.C., Bernath, P.F., Birk, M., Boudon, V., Brown, L.R., Campargue, A., and Champion, J.-P., (2009). The HITRAN 2008 molecular spectroscopic database. *J. Quant. Spectrosc. Radiat. Transf.* 110:533–572.
- Saleh, B.E.A. and Teich, M.C., (2007a). *Fundamentals of Photonics* 2nd ed. Wiley.
- Saleh, B.E.A. and Teich, M.C., (2007b). *Fundamentals of Photonics* 2nd ed. Wiley.
- Sánchez-González, R., Srinivasan, R., Bowersox, R.D.W., and North, S.W., (2011). Simultaneous velocity and temperature measurements in gaseous flow fields using the VENOM technique. *Opt. Lett.* 36:196–198.
- Saskatchewan Ministry of Economy, (2015). New and Active Facilities Report. <http://www.economy.gov.sk.ca/files/RegistryDownloads/NewAndActiveFacilitiesReport.csv> (accessed May 25, 2015)
- Schawlow, A.L. and Townes, C.H., (1958). Infrared and Optical Masers. *Phys. Rev.* 112:1940–1949.
- Schoonbaert, S.B., Tyner, D.R., and Johnson, M.R., (2014). Remote ambient methane monitoring using fiber-optically coupled optical sensors. *Appl. Phys. B*.
- Schultz, I.A., Goldenstein, C.S., Jeffries, J.B., Hanson, R.K., Rockwell, R.D., and Goyne, C.P., (2014). Spatially Resolved Water Measurements in a Scramjet Combustor Using Diode Laser Absorption. *J. Propuls. Power.* 30:1551–1558.
- Sell, J.A., (1984). Quantitative photothermal deflection spectroscopy in a flowing stream of gas. *Appl. Opt.* 23:p. 1586.
- Sell, J.A., (1985). Gas velocity measurements using photothermal deflection spectroscopy. *Appl. Opt.* 24:3725–3735.

- She, C.Y., (1983). Proposal for the measuring molecular velocity vector with single-pulse coherent Raman spectroscopy. *Appl. Phys. B Photophysics Laser Chem.* 32:49–52.
- Sontag, H. and Tam, a C., (1985). Time-resolved flow-velocity and concentration measurements using a traveling thermal lens. *Opt. Lett.* 10:436–438.
- Strand, C.L. and Hanson, R.K., (2015). Quantification of Supersonic Impulse Flow Conditions via High-Bandwidth Wavelength Modulation Absorption Spectroscopy. *AIAA J.* 53:2978–2987.
- Upschulte, B., Miller, M., Allen, M., Jackson, K., Gruber, M., and Mathur, T., (1999). *Continuous water vapor mass flux and temperature measurements in a model scramjet combustor using a diode laser sensor*. In 37th AIAA Aerospace Sciences Meeting & Exhibit. Reno, American Institute of Aeronautics and Astronautics.
- Urquhart, P., (1987a). Transversely coupled fiber Fabry-Perot resonator: theory. *Appl. Opt.* 26:456–63.
- Urquhart, P., (1987b). Transversely coupled fiber Fabry-Perot resonator: theory. *Appl. Opt.* 26:456–63.
- US EPA, (2006). AP 42, 5th ed., Volume I Chapter 7: Liquid Storage Tanks. Research Triangle Park, NC, United States Environmental Protection Agency (US EPA). Available at: <http://www.epa.gov/ttn/chief/ap42/ch07/final/c07s01.pdf> [November 25, 2014]
- Weimer, W.A. and Dovichi, N.J., (1985). Time-resolved crossed-beam thermal lens measurement as a nonintrusive probe of flow velocity. *Appl. Opt.* 24:2981.
- Zapka, W., (1982). Noncontact optoacoustic determination of gas flow velocity and temperature simultaneously. *Appl. Phys. Lett.* 40:1015.
- Zimmermann, M. and Miles, R.B., (1980). Hypersonic-helium-flow-field measurements with the resonant Doppler velocimeter. *Appl. Phys. Lett.* 37:885–887.

Appendix A: Optimization Study

As discussed in Section 4.1, to determine the best possible combination of these frequencies and amplitudes an optimization study was conducted. Starting at $f_{sweep}=100$ Hz, $a_{sweep}=0.28$ V, the first round of parametric experiments (results shown in Figure A.1) initially found a minimum short SD of 0.0386 m/s at $f_m=320$ kHz, and $a_m=0.5$ V. The minimum long SD of 0.008 m/s was found at the same modulation frequency of 320 kHz, and $a_m=0.3$ V. All minima were taken from the actual data points collected, and not from the interpolated points used to draw the optimization surfaces shown in figures. However, because of the irregularity of the long SD surface – which was attributed to the background induced drift as discussed in Section 4.4 – and the comparative smoothness of the short SD surface, the optimized a_m of 0.5 V from the short SD surface was selected for the next step.

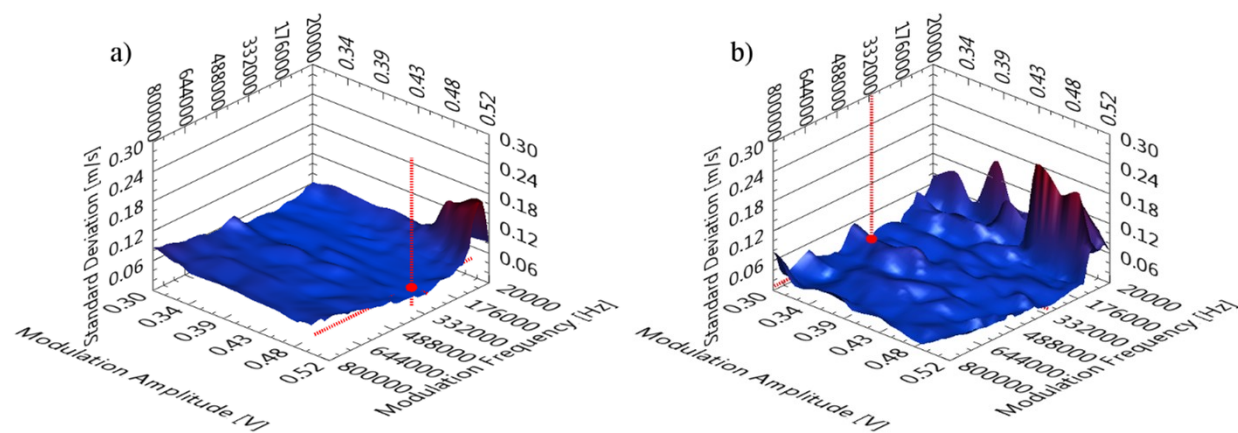


Figure A.1: Surface plots of the parametric optimization of the OTEMS velocity measurement for varying modulation parameters at a fixed sweep of 100 Hz and 0.28 V amplitude. The minimum standard deviation is highlighted by the red point in each sub plot. a) Short SD, minimum of 0.0386 m/s at 320 kHz and 0.5 V. b) Long SD, minimum of 0.008 m/s at 320 kHz and 0.3 V.

The modulation parameters of $f_m=320$ kHz and $a_m=0.5$ V were then used to find new optimal sweep parameters. This resulted in a new minimum short SD of 0.0376 m/s at $f_{sweep}=50$ Hz, $a_{sweep}=0.1$ V. Figure A.2b shows that the minimum long SD of 0.013 m/s occurred at $f_{sweep}=50$ Hz and $a_{sweep}=0.12$ V, which were nearly identical to the optimum short SD values. Once again the long SD surface was more uneven than the short SD surface. From this point forward only the optimums from the short SD were considered. The long SD results are still presented for completeness.

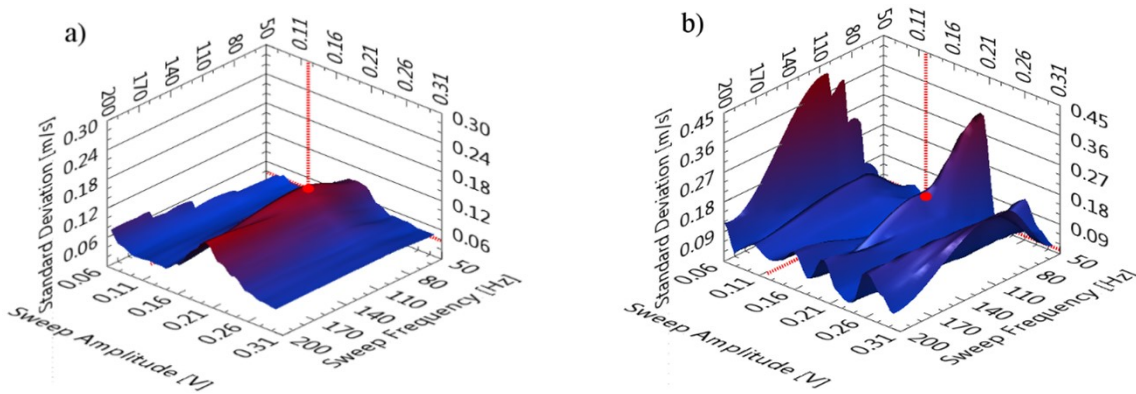


Figure A.2: Surface plots of the parametric optimization of the OTEMS velocity measurement for varying sweep parameters at a fixed modulation of 320 kHz and 0.5 V amplitude. The minimum standard deviation is highlighted by the red point in each sub plot. a) Short SD, minimum of 0.0376 m/s at 50 Hz and 0.1 V. b) Long SD, minimum of 0.013 m/s at 50 Hz and 0.12 V.

The second round of optimization began with the previous sweep parameters of $f_{sweep}=50$ Hz, $a_{sweep}=0.1$ V. Based on the surface from Figure A.3a, a new minimum short SD of 0.0326 m/s was identified at a modulation frequency of 200 kHz and amplitude of 0.28 V.

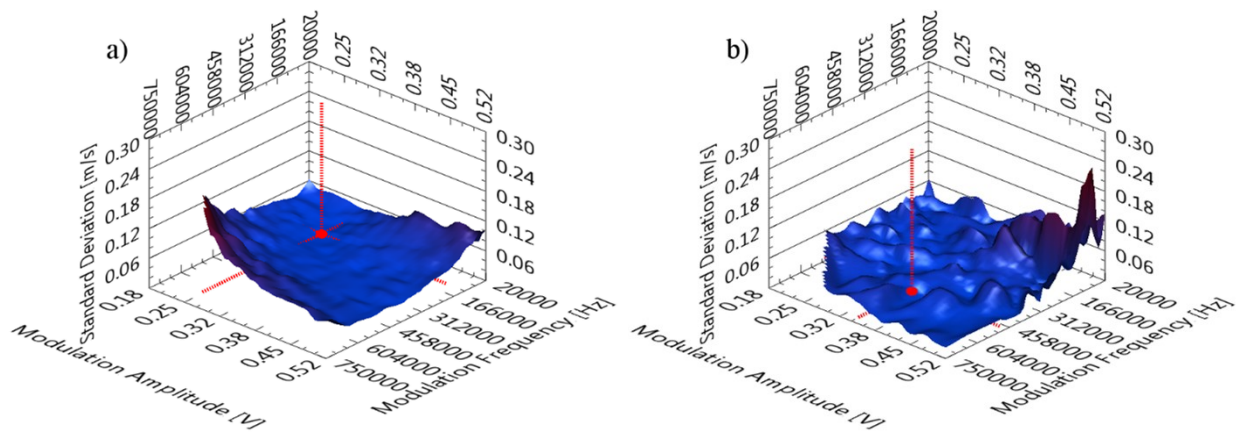


Figure A.3: Surface plots of the parametric optimization of the OTEMS velocity measurement for varying modulation parameters at a fixed sweep of 50 Hz and 0.1 V amplitude. The minimum standard deviation is highlighted by the red point in each sub plot. a) Short SD, minimum of 0.0326 m/s at 200 kHz and 0.28 V. b) Long SD, minimum of 0.011 m/s at 500 kHz and 0.35 V.

The optimization study was concluded with a final investigation of optimum sweep parameters at a modulation frequency of 200 kHz and amplitude of 0.28 V. As seen in Figure A.4a, the minimum short SD (0.0335 m/s) was found at $f_{sweep}=50$ Hz, $a_{sweep}=0.1$ V, thus confirming the previous choice of sweep parameters.

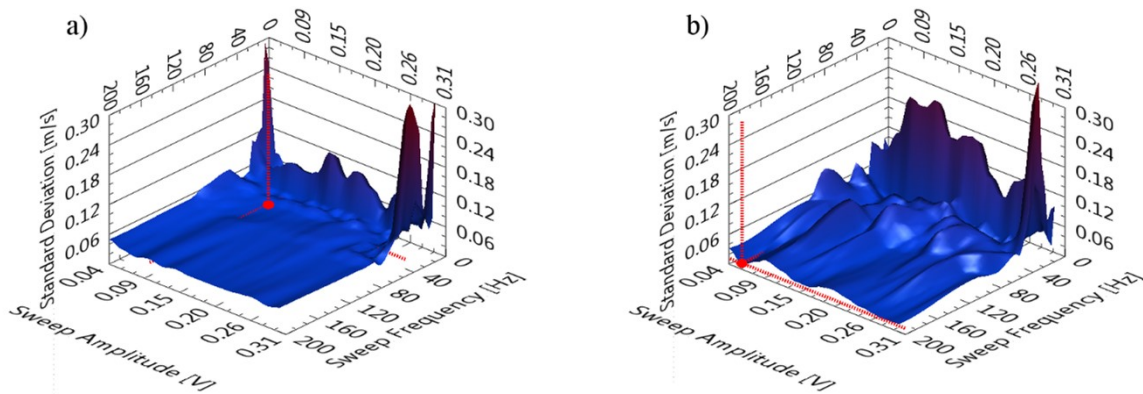


Figure A.4: Surface plots of the parametric optimization of the OTEMS velocity measurement for varying sweep parameters at a fixed modulation of 200 kHz and 0.28 V amplitude. The minimum standard deviation is highlighted by the red point in each sub plot. a) Short SD, minimum of 0.0335 m/s at 50 Hz and 0.1 V. b) Long SD, minimum of 0.012 m/s at 200 Hz and 0.06 V.